Effect of secondary flow and wall collisions on particle-laden flows in 90° pipe bends

Yudong Yan (颜昱东)[1,2], Lee F. Mortimer[2], Bisrat Wolde[2], Michael Fairweather[2], Yanlin Zhao (赵彦琳)[1] and Jun Yao (姚军)[1]

AFFILIATIONS
[1]Beijing Key Laboratory of Process Fluid Filtration and Separation, College of Mechanical and Transportation Engineering, China University of Petroleum-Beijing, Beijing 102249, People's Republic of China
[2]School of Chemical and Process Engineering, University of Leeds, Leeds, LS2 9JT, United Kingdom

[a)] Author to whom correspondence should be addressed: l.f.mortimer@leeds.ac.uk

Abstract

Fully developed, statistically stationary particle-laden turbulent flows in a 90° pipe bend at a moderate Reynolds number are studied using direct numerical simulation coupled to a Lagrangian particle tracking technique. Three populations of particles are studied which are two-way coupled with the carrier phase. The focus is the investigation of the effect of strong curvature on particle transport dynamics across a range of particle inertias. A validation of the carrier phase predictions is performed, with good agreement found with available experimental data. It is demonstrated that the presence of particles notably affects the turbulence statistics of the carrier phase, decreasing the mean fluid velocity in the outer bend while slightly increasing it in the inner bend. Two intriguing phenomena emerge: the presence of a particle void near the inner bend and reflection layers near the outer bend. Centrifugal forces are responsible for driving particles to the outer wall, with some rebounding back into the main body of the flow, and others, influenced by the secondary flow in the plane of the pipe cross-section, converging towards the inner wall before re-entering the central pipe region. These effects dictate the size and shape of the particle void region and the formation of reflection layers due to particle-wall collisions. These two phenomena have a significant influence on the particle distribution in the pipe bend, as well as on the first- and second-order moments of the velocity and acceleration of the particulate phase. Finally, a heat map of particle-wall collision statistics indicates that the effect of the secondary flow on particle distribution and particle-wall collisions is not negligible.

1. Introduction

Particle-laden turbulent flows in 90º pipe bends are widely encountered in industrial processes. In engineering applications, curved pipes have extensive use in various mechanical equipment, including those in the chemical processing and manufacture industries, as well as in agricultural and minerals processing applications. They are commonly employed in processes such as fluid transport and heat exchange within petrochemical systems and gas transmission, as well as in thermal power plants and nuclear power systems. Specific applications include their use in providing flow pathways for centrifugal compressors, configuring flow passages for centrifugal pumps, and directing the flow in fluid transport pipelines. Typically, these flow scenarios involve the complex characteristics of turbulent flow combined with the presence of a discrete particle phase, resulting in multifaceted flow conditions. Due to the curvature of the pipe, fluid within a 90º bend experiences centrifugal forces and unstable pressure gradients. Consequently, flow within such bends is typically characterised by pronounced secondary flows, enhanced pressure drops, as well as flow separation and reattachment. Due to these complex processes, the study of such systems has attracted significant interest in recent years.

In the past two decades a significant amount of experimental and simulation work has been conducted. Bradshaw and Young [1] and Kalpakli Vester et al. [2] provided extensive and detailed reviews of turbulent flows in curved pipes. In terms of experiments, the key findings consistently reported across various studies include the observation that the mean streamwise velocity increases along the inner wall of the pipe

bend at 30º, which is also the position where Dean vortices are formed. Dean vortices are distinctive fluid patterns occurring within flows in curved pipes that emerge due to an adverse pressure gradient generated from the curvature which decreases the velocity close to the convex wall, and increases it towards the outer wall of the pipe. This causes the high-velocity fluid in the centre of the pipe to deflect outward along the pipe bend, forming two counter-rotating vortices, with the mean flow observed to deviate from a fully developed turbulent profile at upstream distances of approximately one pipe diameter. Sudo et al. [3] employed a hot-wire anemometry technique to measure the mean velocity and Reynolds stress in a 90° circular cross-section pipe bend at a bulk Reynolds number of 6×10^4, with their detailed findings on the characteristics of bend flows widely cited by subsequent researchers. Shirvan [4] conducted a series of single-phase turbulent flow experiments using hot-wire measurements within curved pipes. It was noted that in a 90° curved pipe, the root mean square (r.m.s.) of the axial velocity fluctuations is greater along the inner wall of the bend and smaller along the outer wall. Takamura et al. [5] conducted flow field visualisation within a single short elbow pipe at relatively high Reynolds numbers ($0.3 \times 10^6 - 1.0 \times 10^6$) using particle image velocimetry. Their experimental results showed that flow structures are not strongly dependent on the Reynolds number in this range. However, the positions of the flow separation and reattachment points change slightly with an increase in Reynolds number which causes expansion of the separation region and a simultaneous increase in velocity fluctuations. Other researchers [6, 7] have employed proper orthogonal decomposition of their experimental data, although their results were not conclusive.

As highlighted in the review paper by Kalpakli Vester et al. [2], accurately capturing the spatially evolving turbulent flow within 90° bends through experimental means can be challenging. Utilising numerical simulations for studying such flows can therefore offer valuable insights into turbulent flows in bends.

In terms of numerical simulations, a large number of Reynolds-averaged Navier-Stokes (RANS) simulations of flow in curved pipes have been reported. These researches mainly adopt an engineering perspective, preferring to simulate high Reynolds number conditions and focusing on parameters such as pressure drop, friction and average statistics. Duarte et al. [8] used an unsteady RANS approach to study wear by particle transport in 90° pipe bends which is of significant concern in industry. Kim et al. [9] employed a variety of RANS models available in OpenFOAM to simulate the turbulent flow field in a 90° bend, with results indicating that the renormalisation group k-ε turbulence model outperforms other turbulence models, particularly in calculating primary streamwise velocity and secondary swirling velocity profiles. RANS models are computationally efficient and provide reasonable accuracy for mean turbulence statistics, making them well-suited for industrial simulations. However, they are unable to accurately capture flow field fluctuations. For pipes with bends, the influence of centrifugal forces caused by the inherent curvature of the streamlines affects not just the bulk flow near the pipe centre but also regions close to the walls. This substantial anisotropy in the flow deviates from the quasi-equilibrium conditions typically assumed in traditional turbulence modelling, such as eddy viscosity models [10]. Direct numerical simulation (DNS) and large eddy simulation (LES) can capture turbulent fluctuations

by resolving the instantaneous turbulent flow field, but the range of relevant length and time scales which must be resolved significantly increases with Reynolds number. This causes DNS to be unfeasible for most engineering applications that typically involve very high Reynolds numbers, although LES is frequently possible. In general, however, DNS and LES are generally employed for investigating low Reynolds number flows in simple geometries, such as pipes, channels and ducts. In particular, the implementation of periodic boundary conditions can effectively reduce the size of the geometric computational domain, thereby reducing the computational cost for statistically steady, fully developed turbulent flows in these geometries. Hüttl and Friedrich [11, 12] conducted DNS studies on the impact of curvature on the mean flow and velocity fluctuations for low curvature bends. In a more recent study, Noorani et al. [13] applied periodic boundary conditions at the inlet and outlet of a curved pipe to obtain a spatially stable flow utilising the spectral element code Nek5000, investigating the impact of curvature on turbulence with results showing that curved pipes tend to have a higher critical Reynolds number for transition to turbulence than straight pipes, and with partial laminarisation observed along the inner surface of pipes with high curvature. However, for typical spatially developing turbulence akin to what is found in 90° curved pipes in practice, there is a scarcity of DNS and LES studies, with such DNS studies only becoming available in recent years. Wang et al. [14] and Hufnagel et al. [15] investigated the unsteady fluid motions downstream of the bend and used proper orthogonal decomposition to analyse swirl-switching phenomena, a low-frequency oscillatory phenomenon which affects the Dean vortices, which indicated that the flow in the bend

is complex and that detailed three-dimensional characterisation of the swirl-switching modes is necessary to understand the cause of these oscillations.

Previous research efforts on particle transport within straight pipes have yielded significant achievements. It is well-known that the transport of small inertial particles in wall turbulence exhibits a phenomenon known as turbophoresis, which involves the accumulation of heavy particles near the wall due to turbulence inhomogeneity and gradients in mean turbulence kinetic energy profiles [16]. This effect results in significantly higher particle concentrations near the wall compared to the central region of the pipe. Another specific occurrence during the dispersion of heavy particles is small-scale clustering, where particles tend to aggregate in regions with high turbulence kinetic energy dissipation rates [17]. In contrast to typical turbulence effects, this phenomenon, often referred to as particle preferential concentration, is observed in various turbulent flows containing heavy particles, whether they are homogeneous or inhomogeneous. Additionally, both phenomena are related to the particle Stokes number based on the Kolmogorov scale, with studies highlighting that these phenomena are most prominent when the Stokes number is ~25 in both channel [18] and duct [19] flow. This is due to the coherent structures near the wall in turbulent flows and their associated vortex effects, which selectively affect particles based on their inertia. When the relaxation time of particles aligns with the characteristic timescale of the coherent structures of turbulence, the particle concentration near the wall reaches its maximum. Previous research has primarily focused on Stokes numbers up to 100. In this work we consider larger particles, with Stokes numbers based on the viscous scale ranging from

100 to 1000.

Regarding particle motion in curved pipes, besides some efforts focusing on industrial applications such as particle transport efficiency and pipeline erosion, studies of complex turbulent two-phase phenomena in pipe bends are rare [20]. Noorani et al. [21] note that in statistically stationary, fully developed turbulent flows within moderately curved pipes, particle motion is significantly influenced by Dean vortices, causing particles to follow the contours of the secondary flows. In certain regions within the pipe, there may even be no particle flux into these regions, resulting in what is known as particle voids. Noorani et al. [20] also demonstrated, through the statistical analysis of particle flux, a significant increase in accumulation caused by secondary motions that drive particles towards the pipe's central regions while simultaneously pushing them towards the outer pipe bend. Yan et al. [22, 23] conducted studies on particle-laden flows within 90º pipe bends using LES. Their findings indicated that particle preferential clustering at the Dean inner and outer stagnation points varies, and electrostatic effects may enhance particle aggregation in the near-wall region. So far, these studies of particle-laden turbulent flows within curved pipes have been limited to one-way coupling between the fluid flow and the particles, and there is a notable lack of research on particle-laden flow within 90º pipe bends using two-way coupled DNS.

In this paper, DNS is used to study turbulence modulation and particle turbulent statistics in a 90º pipe bend. To the authors' knowledge the present study is the first DNS of a particle-laden turbulent flow in a 90º pipe bend using two-way coupling at a realistically high Reynolds number. The paper is organized as follows: in Section 2, the

governing equations and numerical methods employed are briefly reviewed, as well as the flow configuration. In Section 3.1, the predicted single-phase flow field is visualized and validated against available experimental data, followed by an analysis of particle-turbulence modulation. In Section 3.2, an extensive examination of the particulate phase is performed, encompassing the temporal evolution of particle concentration, spatial distribution, particle velocities, velocity fluctuations, and particle-wall collisions. Finally, Section 4 provides some concluding remarks.

2. Numerical simulation

2.1 Fluid motion

Direct numerical simulation was carried out to obtain an accurate carrier phase flow field representing a fully developed incompressible Newtonian turbulent flow in a pipe with a 90º bend. In this study, the motion of the carrier phase is simulated using the spectral element method solver NEK5000 [24], which is written in FORTRAN 77 and C, and parallelized using MPI techniques. Based on the spectral element method, the computational domain is subdivided into hexahedral local elements, and the solution is computed at the Gauss-Lobatto-Legendre quadrature points utilizing Lagrange polynomials of order N within each element. Because of its high-order accuracy and effective parallelization capabilities, this code has gained broad acceptance and validation in numerous DNS applications for wall-bounded flows [13, 18, 19, 25].

2.1.1 Governing equations for fluid phase

For the incompressible continuous phase, the governing dimensionless Navier-

Stokes equations, are given as follows:

$$\nabla \cdot \boldsymbol{u}^* = 0 \tag{1}$$

$$\frac{\partial \boldsymbol{u}^*}{\partial t^*} + (\boldsymbol{u}^* \cdot \nabla)\boldsymbol{u}^* = -\nabla p^* + \frac{1}{Re_b}\nabla^2 \boldsymbol{u}^* + \boldsymbol{f}^* \tag{2}$$

It is worth noting that each term in these equations is dimensionless, signified by the superscript "*". In the present study, velocity, length, time and force terms are non-dimensionalized using the bulk velocity of the fluid u_b, pipe diameter d, d/u_b and u_b^2/d, respectively. Therefore, in the above equations, $\boldsymbol{u}^*$ is the fluid velocity with $\boldsymbol{u}^* = \boldsymbol{u}/u_b$, p^* is the fluid pressure, $p^* = p/(\rho u_b^2)$, Re_b is the bulk Reynolds number, defined as $Re_b = u_b d/\nu$, and ν and ρ are the fluid kinematic viscosity and fluid density, respectively. $\boldsymbol{f}^*$ represents an extra forcing term, $\boldsymbol{f}^* = \boldsymbol{f}d/u_b^2$, which is the two-way coupling feedback fo1rce from the particulate phase to the fluid. More details about the spectral element method and the numerical code can be found elsewhere [24]. In addition, unless otherwise specified, the superscript "+" in this work indicates variables made dimensionless using viscous scales, i.e. $\boldsymbol{u}^+ = \boldsymbol{u}/u_\tau$, $\boldsymbol{x}^+ = \boldsymbol{x} \cdot u_\tau/\nu$ and $t^+ = tu_\tau^2/\nu$, where u_τ is the mean shear velocity, which is defined as $u_\tau = \sqrt{\tau_w/\rho}$, and τ_w is the mean wall shear stress, which is based on the mean wall shear stress in the upstream straight pipe.

2.1.2 Flow configuration and numerical settings

As the turbulence within a 90º pipe bend exhibits asymmetric spatial development characteristics, any simulation cannot employ periodic boundary conditions at the inlet and outlet as is typically done in straight pipe simulations. Therefore, for simulations involving the curved section, the inlet boundary conditions are of paramount

importance. An auxiliary simulation of a straight cylindrical pipe with periodic boundary conditions at the inlet and outlet was therefore undertaken to generate realistic time-dependent turbulent inflow data for the pipe bend computations. The entire simulation is therefore divided into two parts: the auxiliary simulation of a straight pipe and the main simulation of the 90º pipe bend, as shown in Figure 1. For the straight pipe section, once the turbulent flow had reached a fully developed steady state and the predictions validated, a continuous time series of instantaneous velocity distribution data at the outlet plane was extracted. This data was subsequently employed as the inflow boundary for the pipe bend simulation. In the present work, we used both Cartesian (x, y, z) and cylindrical (r, φ, s) coordinate systems. In both cases, the coordinate origin is located at the centre of the inlet plane of the pipe bend. For the Cartesian coordinate system, the z axis is aligned with the streamwise direction, the y axis with the vertical direction and the x axis with the spanwise direction. For the cylindrical coordinate system, s indicates the streamwise direction, and φ and r represent the circumferential and radial directions, respectively. The length of the straight pipe was set to $12.5d$, which is sufficiently long to resolve the largest streamwise structures in a turbulent pipe flow [26]. In the main pipe bend simulation, the upstream and downstream elbows were restricted to lengths of $2d$ and $4d$, respectively, as the flow has been shown to deviate from a fully developed turbulent profile at upstream distances of approximately $1d$ [2, 3, 27], and since this work focuses more on the flow field of the bend section. No-slip boundaries were imposed on all the pipe walls, and outflow boundary conditions were imposed on the outlet plane of the pipe bend

computational domain. The radius of curvature, R_c, of the bend was set to $2.4165d$, which is in-line with the experimental work of Shirvan [4] used below to validate the single-phase DNS predictions.

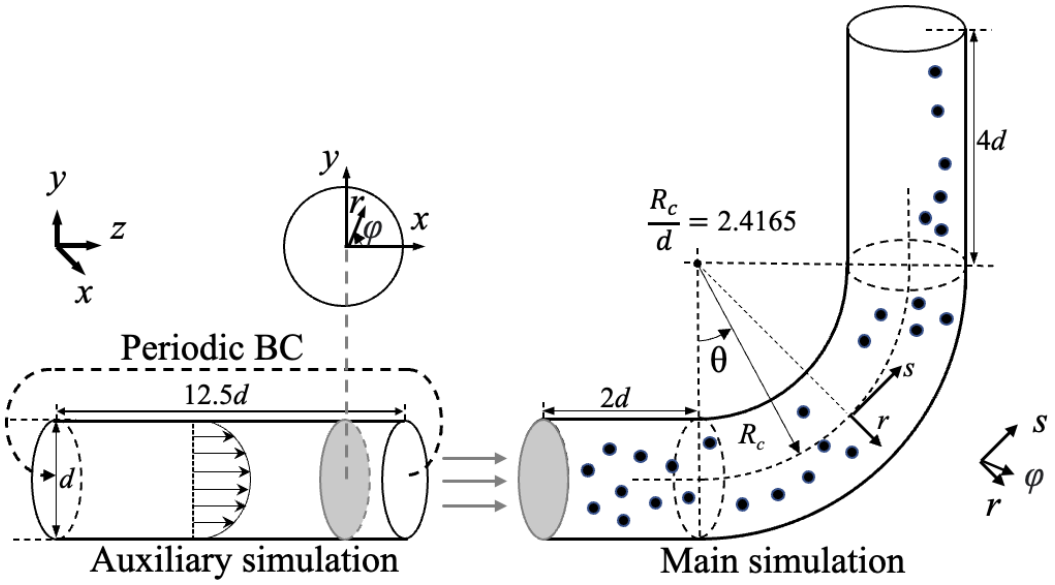

Figure 1. Schematic diagram of the computational domain.

The bulk Reynolds number was set to $Re_b = 13{,}960$, in-line with Shirvan [4], with the corresponding shear Reynolds number $Re_\tau = 838$, where $Re_\tau = u_\tau d/\nu$. For this geometric configuration, the Dean number is $6{,}350$, which is defined as $De = Re_b\kappa$, where κ is the curvature parameter defined as $\kappa = \sqrt{r_a/R_c}$. The Dean number is used to indicate the intensity of secondary flows in a bend. At the given Reynolds number, the numerical grid on part of the cross-sectional and vertical planes through the pipe are shown in Figure 2. The cross-sectional mesh was created using a decomposition approach tailored for cylindrical geometries within a Cartesian solver, as depicted in Figure 2. The final mesh was achieved through analytical morphing of the straight pipe

mesh. Therefore, the cross-sectional mesh of the straight pipe and curved pipe sections is consistent. Additionally, to attain the desired numerical resolution, additional grid refinement was applied to each element in the pipe bend. The mesh spacing was therefore designed to keep $\Delta r^+_{wall} \leq 1$, Δr^+_{max}, $\Delta(r_a\varphi)^+_{max} \leq 10$ and $\Delta s^+_{max} \leq 20$ [28]. The polynomial order was set to 7, which means there were 8^3 points in each element. The final number of equivalent grid points was 22×10^6, and the grid spacing in three directions was $\Delta r^+ \in (0.85, 9.22)$, $\Delta(r_a\varphi)^+ \in (3.33, 9.25)$ and $\Delta s^+ \in (3.91, 16.67)$. The characteristics of the computational mesh are summarized in Table 1, with equivalent numerical resolution used in the straight pipe simulation. A fixed fluid solver time step was used (Δt^*=0.0005), with the corresponding Courant number always less than 0.5. The time step of the particle solver was also set to be equal to the DNS solver time step.

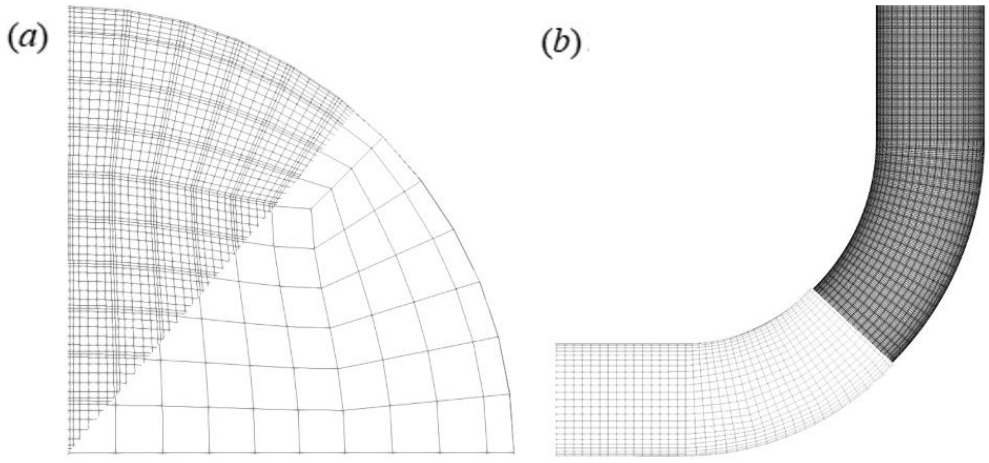

Figure 2. Grid representation of straight pipe and pipe bend: (a) a quarter of the cross-sectional plane of both pipes, and (b) a vertical plane through the pipe bend. Here, element boundaries and Gauss-Lobatto-Legendre points are shown in the darker regions.

Table 1. Resolution details for the numerical mesh used in the pipe bend simulations.

Re_b	De	No. of elements	No. of grid points	Δr^+	$\Delta(r_a\varphi)^+$	Δs^+
$\mathbf{13,960}$	6,350	43,008	22,020,096	$(0.85, 9.22)$	$(3.33, 9.25)$	$(3.91, 16.67)$

2.2 Particle motion

In the present work, particle motion was determined using Lagrangian particle tracking (LPT) in which equations of motion are solved for each particle, concurrently with the fluid flow solver. It is based on the point-particle approach, as the particle size was less than the smallest Kolmogorov scale present within the turbulent flow [29]. All particles are considered as spherical point sources with the same physical properties. The motion of particles in turbulent flows is typically governed by several forces, including the drag, lift, added-mass, pressure gradient, Basset history, gravity and buoyancy forces. Among these forces, drag is acknowledged as the most predominant force governing particle motion in particle-laden flows. Typically, when considering LPT methods in such flows, both drag and lift forces are taken into account. According to Armenio and Fiorotto [30], the pressure gradient force can be ignored when the ratio of the particle to fluid density is greater than $\mathcal{O}(10^3)$. In the current study, the discrete-phase particles and carrier-phase materials are set as polypropylene (with a density of $850kg\ m^{-3}$) and air (with a density of $1.255kg\ m^{-3}$), resulting in a density ratio of $\rho_p^* = \rho_p/\rho = 694$. Although this density ratio is quite substantial, it is important to consider pressure gradient forces due to the significant pressure differences between the inner and outer walls within the pipe bend flow. On the other hand, the Basset

history force is not considered because its contribution is significantly smaller than that of the other forces when the particle size d^+ is less than $\mathcal{O}(1)$ [31], and has been found to be negligible for particle-to-fluid density ratios > 500 [32]. The particle size of the largest particles ($d_p^+ = 5.1$) is on the order of the characteristic scale of the viscous sublayer and therefore attention in the analysis must take into account the assumption that for the largest particles, the dynamics in that region are driven primarily by inertia and collisions, with little effect of the hydrodynamics from the local fluid field. Additionally, gravity has a significant impact on particle motion that cannot be overlooked. Numerous studies have reported that even for very small particles, gravity plays a substantial role in particle deposition [16, 33-35]. In summary, this study considers the drag, lift, added-mass, pressure gradient, and gravity and buoyancy forces.

2.2.1 Governing equations for particle phase

Considering the simplifications mentioned above, and to facilitate integration with Nek5000, the particle motion equations are solved in dimensionless form using the same principles as for the fluid phase. The equations of motion can be expressed in the following forms:

$$\frac{d\boldsymbol{x}_p^*}{dt^*} = \boldsymbol{u}_p^*, \tag{3}$$

$$\frac{d\boldsymbol{u}_p^*}{dt^*} = \frac{1}{M_{VM}}\left[\underbrace{\frac{3C_D\left|\boldsymbol{u}^* - \boldsymbol{u}_p^*\right|}{4d_p^*\rho_p^*}\left(\boldsymbol{u}^* - \boldsymbol{u}_p^*\right)}_{drag} + \underbrace{\frac{3C_L}{4\rho_p^*}\left(\boldsymbol{u}^* - \boldsymbol{u}_p^*\right)\times\boldsymbol{\omega}^*}_{lift} + \underbrace{\frac{1}{2\rho_p^*}\frac{D'\boldsymbol{u}^*}{Dt^*}}_{virtual\ mass} + \underbrace{\frac{1}{\rho_p^*}\frac{D\boldsymbol{u}^*}{Dt^*}}_{pressure\ gradient} + \underbrace{\frac{1}{Fr}\left(1-\frac{1}{\rho_p^*}\right)\hat{\boldsymbol{g}}}_{gravity\&buoyancy}\right], \tag{4}$$

where variables with subscript p represent parameters associated with the particle phase. The term $\boldsymbol{\omega}^*$ is the dimensionless local fluid vorticity at the particle position

which is defined as $\boldsymbol{\omega}^* = \nabla \times \boldsymbol{u}^*$. C_D and C_L represent the Stokes drag coefficient and slip-shear lift coefficient, respectively, given by the following equations:

$$C_D = \begin{cases} 24/Re_p & Re_p \leq 0.5 \\ 24/Re_p \cdot \left(1 + 0.15Re_p^{0.678}\right) & 0.5 < Re_p < 1000 \\ 0.44 & Re_p \geq 1000 \end{cases}, \quad (5)$$

where Re_p is the particle Reynolds number which is defined as $Re_p = Re_b d_p^* |\boldsymbol{u}^* - \boldsymbol{u}_p^*|$. The Saffman-Mei coefficient [36, 37] is used to account for lift, which incorporates corrections to the standard Saffman coefficient to account for a wider range of particle Reynolds numbers, given as:

$$C_L = \frac{4.1126}{Re_G^{0.5}} f(Re_p, Re_G)), \quad (6)$$

where Re_G is the Reynolds number of the local shear flow, defined as $Re_G = Re_b d_p^* 2|\boldsymbol{\omega}^*|$, and the other variables are given as:

$$f\left(Re_p, Re_G\right) = \begin{cases} (1 - 0.3314\alpha^{0.5})e^{-\frac{Re_p}{10}} + 0.3314\alpha^{0.5} & 0 \leq Re_p \leq 40 \\ 0.0524\left(\alpha Re_p\right)^{0.5} & Re_p > 40 \end{cases}, \quad (7)$$

$$\alpha = 0.5\frac{Re_G}{Re_p}. \quad (8)$$

For the virtual mass and pressure gradient forces, the operators D/Dt^* and D'/Dt^* represents the standard material derivatives of the fluid phase and that observed by the particles, i.e. $D/Dt^* = \partial/\partial t^* + \boldsymbol{u}^* \cdot \nabla$ and $D'/Dt^* = \partial/\partial t^* + \boldsymbol{u}_p^* \cdot \nabla$. In addition, M_{VM} indicates the added mass correction, which is obtained from $M_{VM} = 1 + 1/2\rho_p^*$. Fr is the Froude number, defined as $Fr = u_b^2/gd$, where g and $\hat{\boldsymbol{g}}$ are the gravitational acceleration and a unit vector in the direction of gravitational attraction. In this paper the direction of gravity is the negative direction of the y-axis.

To account for two-way coupling, for a given mesh cell, the mean forces applied to each particle during a numerical timestep are also distributed to the local fluid cell.

The feedback force of particles to the fluid is calculated by the Eq. (9), which was introduced as an additional term in Eq. (2):

$$\boldsymbol{f}_i^* = -\frac{1}{V_{i,cell}^*(1-\Phi_p)}\sum_{j=1}^{n}\left(\frac{\partial \boldsymbol{u}_{p,j}^*}{\partial t^*}_{drag} + \frac{\partial \boldsymbol{u}_{p,j}^*}{\partial t^*}_{lift}\right). \quad (9)$$

For a given computational mesh cell i, $V_{i,cell}^*$ is the volume of the cell, and n is the total number of particles in the cell. The drag and lift forces of the particles are added to the fluid's momentum equation as feedback forces on the fluid, indicated by the partial differential subscripts. The pressure gradient and virtual mass contributions were neglected when calculating the feedback force, since their proportional magnitudes will be insignificant due to the high density ratio considered here ($\rho_p^* = 694$) and their inverse scaling with that parameter. The approach that considers the two-way coupling effect is most commonly known as the particle-source-in-cell (PSIC) method. [38]

2.2.2 Lagrangian particle tracking numerical solution method

The Lagrangian point-particle technique was integrated with Nek5000 to process the simulation of particle motion. The LPT code was initially integrated into Nek5000 for simulating gas-solid two-phase flows in channels by Mortimer et al. [18]. Subsequently, it was adopted by other researchers for simulations in duct [19] and pipe flows [35]. It has been validated for various cases and shown to be applicable in a wide range of scenarios. In this work, the code was adapted to predict particle flows in pipe bends.

Particle motion was calculated upon completion of the fluid phase solver at every timestep. In the LPT code, Eqs. (3) and (4) were numerically integrated using a fourth-order Runge-Kutta scheme to compute each particle's updated position and velocity at

every time step, and the particle time step was set to be identical to that of fluid phase, which was much smaller than the smallest particle relaxation time to ensure that particle trajectories were fully resolved. A large number of particles were randomly injected in to the computational domain after the fluid flow field was demonstrated to reach a fully developed state. The initial velocity of each particle was set equal to that of the fluid at the centre of the particle, obtained using spectral interpolation methods. Particle-wall interactions were modelled using fully elastic collisions, such that a particle's wall-normal velocity was reversed when it reached the solid boundary, justified due to the fundamental exploratory aim of the study, and to focus solely on the effects of particle trajectories on turbulence without accounting for loss of energy through other means. If a particle-wall collision is detected in a certain time step, the bisection method is used in that time step Δt to find the precise time when the collision occurs, and then the particle information after the collision is updated. For each particle exiting the computational domain of the pipe bend, a new particle is randomly introduced at the inlet plane of the pipe bend simulation to maintain a constant volume fraction of particles throughout the computational domain of the main simulation.

One of the critical parameters in particle-laden flows is the particle Stokes number, St, which indicates particle relaxation time relative to a particular fluid time scale and measures the significance of particle inertia. The Stokes numbers based on the viscous scale (St^+) and integral scale (St_b) are given by:

$$St^+ = \frac{\tau_p}{\tau_\nu} = \frac{\rho_p d_p^2/18\mu}{\nu/u_\tau^2} = Re_\tau^2 \frac{d_p^{*2}\rho_p^*}{18}, \tag{10}$$

$$St_b = \frac{\tau_p}{\tau_b} = \frac{\rho_p d_p^2/18\mu}{d/u_b} = Re_b \frac{d_p^{*2}\rho_p^*}{18}, \quad (11)$$

where τ_p is the particle relaxation time, given by $\tau_p = \rho_p d_p^2/18\mu$, and τ_v and τ_b are the fluid viscous and fluid bulk timescales, respectively.

Three populations of particles were simulated in the present study, with corresponding shear Stokes numbers St^+ of 100, 500 and 1000. For all populations, the conditions of the carrier phase were the same, with the bulk flow Reynolds and Dean numbers fixed to $Re_b = 13{,}960$ and $De = 6{,}350$. The density ratio of the particles to the fluid in all cases was fixed at 694. Despite the simulations being at a reasonably large particle volume fraction, with $\Phi_v = 1 \times 10^{-3}$, only two-way coupled simulations were performed since the effects associated with four-way coupling are not the primary focus of this paper, but will be considered in a future study. The various particle populations and their corresponding parameters can be found in Table 2.

Table 2. Parameters relevant to the particle simulations.

St^+	St_b	Re_b	Re_τ	De	d_p^*	$d_p(\mu m)$	ρ_p^*	Φ_v	N_p
100	2				1.93×10^{-3}	115			1,644,480
500	10	13,960	838	6,350	4.30×10^{-3}	258	694	10^{-3}	146,880
1000	20				6.08×10^{-3}	365			52,000

3. Results and discussion

In this section, we present the continuous phase flow field visualization and validations results, and particle characterization results in the 90º bend. Firstly, the flow field in the full pipe is fully validated to ensure the reliability of the computational method. We then focus on the turbulent secondary flows in the pipe bend and the

resulting statistical characteristics of the particles.

3.1 Carrier phase

It is essential to gain a comprehensive understanding of the turbulence in the carrier phase. To achieve this, this section describes and discusses the key characteristics of the turbulent flow in the bend configuration. Due to the asymmetric spatial development of the turbulent flow within the pipe bend, spatial averaging is not applicable.

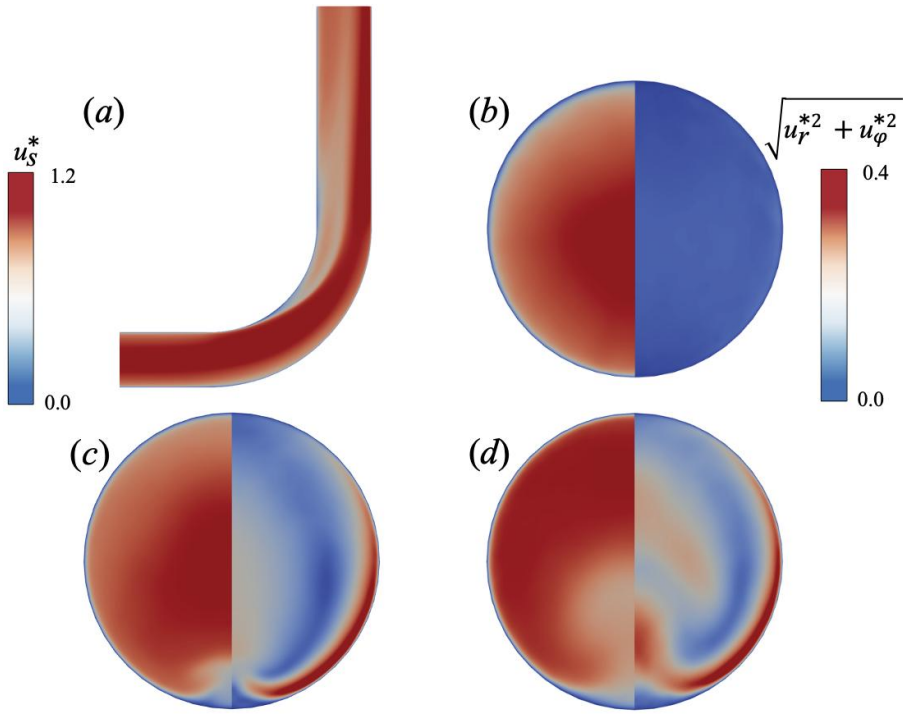

Figure 3. Flow field visualization: (a) mean streamwise velocity on vertical plane (plane $x = 0$), and mean streamwise velocity (left section) and mean secondary velocity (right section) evolution of carrier phase in bend cross-section on planes at: (b) $\theta = 0°$, (c) $\theta = 45°$, and (d) $\theta = 90°$. Outer wall on top of the figure and inner wall on the bottom.

Figure 3 shows snapshots of mean velocities for flows within the pipe bend.

Subplots (a)-(d), respectively, display the vertical mid-plane ($x = 0$) and cross-sections at different θ within the pipe bend, denoted as $\theta = 0°, 45°$ and $90°$. The left and right parts of the latter plots represent the streamwise and secondary velocity distributions, respectively. Qualitatively, it is evident that the turbulence within the pipe bend has reached a statistically stable state, capturing the typical secondary flows in the bend. The streamwise velocity along the inner wall of the bend forms a concavity. The secondary flow develops from the outer wall towards the inner wall along the sidewall, ultimately forming opposing rotating vortex structures known as Dean vortices. This configuration has been extensively studied and reported by numerous researchers in pipe bend flows [14, 39-41]. This phenomenon emerges due to the pressure difference between the inner and outer walls of the pipe induced by the centrifugal forces caused by the pipe curvature, with the magnitude of the secondary flow closely associated with the bend curvature. Yan et al. [23] noted that for the first type of Prandtl secondary flow in a 90º bend, the magnitude of the secondary flow is primarily linked to its curvature. Greater curvature results in stronger secondary flows. In a 90º bend with a curvature constant $\kappa = 0.5$, the maximum magnitude of the secondary flow can reach up to 55% of the bulk velocity, while in this study, with a curvature constant $\kappa = 0.45$, the maximum secondary flow is approximately 40% of bulk velocity. Additionally, the flow in the bend continuously evolves, with the peak magnitude of the secondary flow occurring around $\theta = 48°$, followed by a gradual attenuation downstream with stable Dean vortices.

Because of this, all statistical results for the pipe bend flow presented below have

been averaged over time. We use dimensionless time t^* based on the bulk scale (normalised by $2r_a/u_b$) to indicate simulation time. Therefore, unless explicitly stated otherwise, the following analysis only uses time averaged results, represented by variables with symbol $\langle\cdot\rangle$ (although averaging is implied in r.m.s. value). In contrast, for the straight pipe simulation, this symbol indicates time and spatial averaging in the streamwise direction.

3.1.1 Validation

To quantitively validate the accuracy of the flow field predictions, we present a comparisons of the present results with those of previous studies. The validation includes two parts, for the straight pipe and the pipe bend. Firstly, the straight pipe results of the auxiliary simulation were validated against the DNS calculations of El Khoury et al. [25]. The bulk Reynolds number of the present simulation was $\mathrm{Re_b}=13{,}960$, with the present results compared with those of El Khoury et al. [25] at bulk Reynolds numbers of 11700 and 19000. The results are shown in Fig. 4. The mean streamwise velocity shows very good agreement with the latter simulations. The second-order turbulence statistics, i.e. the normal and shear stress, show the Reynolds number dependence which has been reported by several previous studies [23, 25]. This work demonstrated that the velocity fluctuations in turbulent pipe flows increase with the Reynolds number but exhibit overlap within the viscous sublayer, in line with the results of Fig. 4. However, in the region $(1\text{-}\mathrm{r}/\mathrm{r_a})^+>10$, this discrepancy gradually becomes more pronounced, and the peak positions of the normal and shear stresses move slightly away from the wall with increasing Reynolds number. The present results also

demonstrate this Reynolds number effect. Based on these comparisons, the agreement found gives confidence in the predictions of the continuous phase flow field.

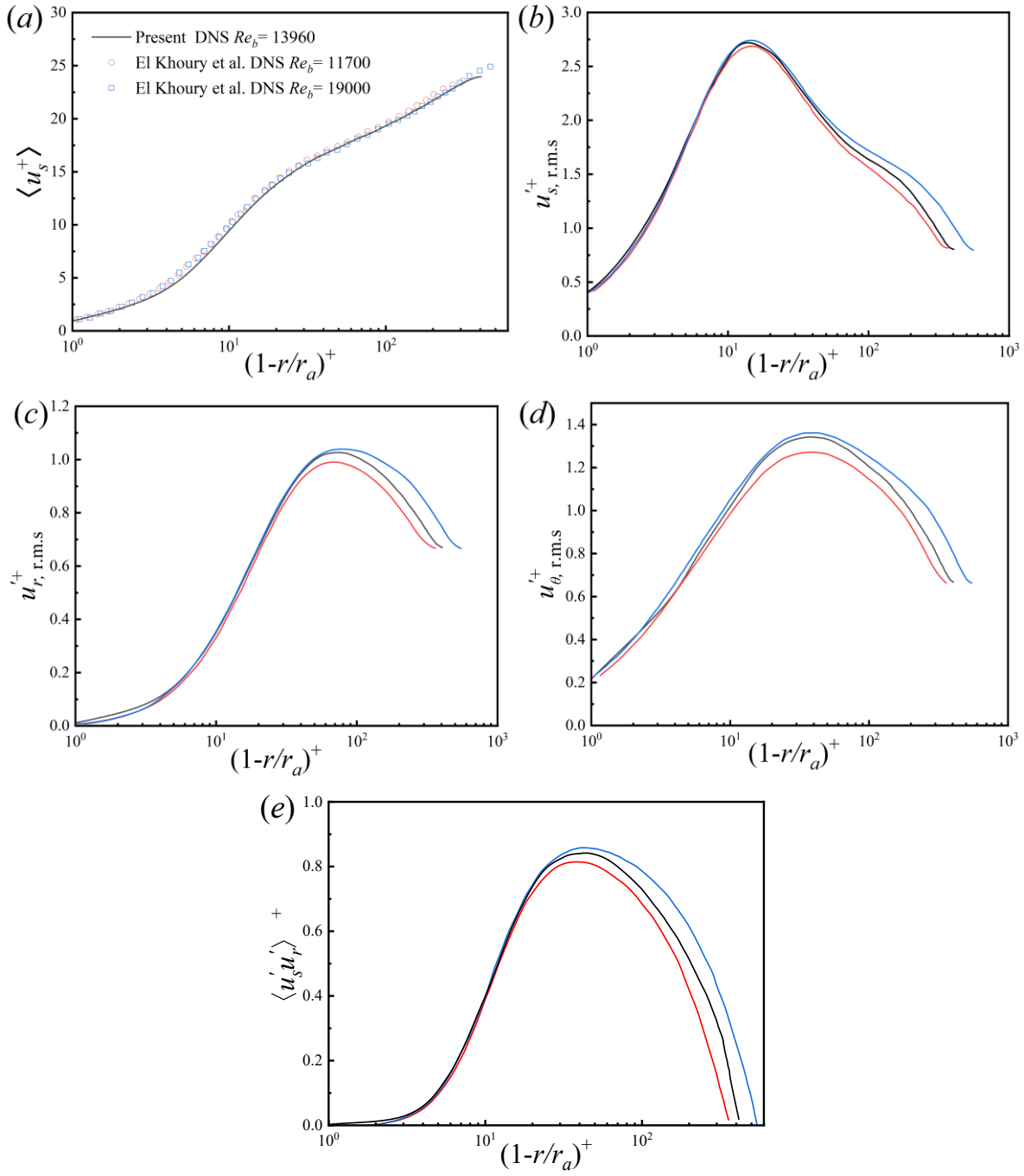

Figure 4. Velocity statistics in the straight pipe at $Re_b = 13{,}960$ compared with the DNS of El Khoury et al. [24]: (a) streamwise mean velocity, (b) streamwise normal stress, (c) radial normal stress, (d) azimuthal normal stress, and (e) Reynolds shear stress.

For the 90º pipe bend flow, the present DNS results for the single-phase were validated against the experimental data of Shirvan [4]. Figure 5 displays the mean velocity and intensity of turbulence profiles along the centreline at downstream distances of $0.5d$ and $1.5d$ in the cross-section of the bend. Both the mean and r.m.s. velocity predictions demonstrate acceptable agreement with the data. In particular, the current simulation captures the influence of the secondary flows on the velocity fluctuations. Due to the convergence of the two counter-rotating secondary flows along the sidewalls near the stagnation point on the inner wall, there is a peak in the intensity of turbulence in the central region of the bend. This peak gradually shifts towards the outer wall downstream. Interestingly, in the studies of Noorani et al. [13, 21] of an infinitely long curved pipe with a stable secondary flow, this peak was not observed. Some deviation from the results presented here is to be expected, however, due to the intrusiveness of the hot-wire anemometer technique used by these authors to acquire measurements.

3.1.2 Turbulence modulation by particles

It should first be noted that, to the authors' knowledge, no experimental data or predictions of numerical simulations exist for particle-laden pipe bend flows similar to that considered here against which the present predictions could be validated. This section therefore presents results on the impact of the particles on the flow from the present simulations alone.

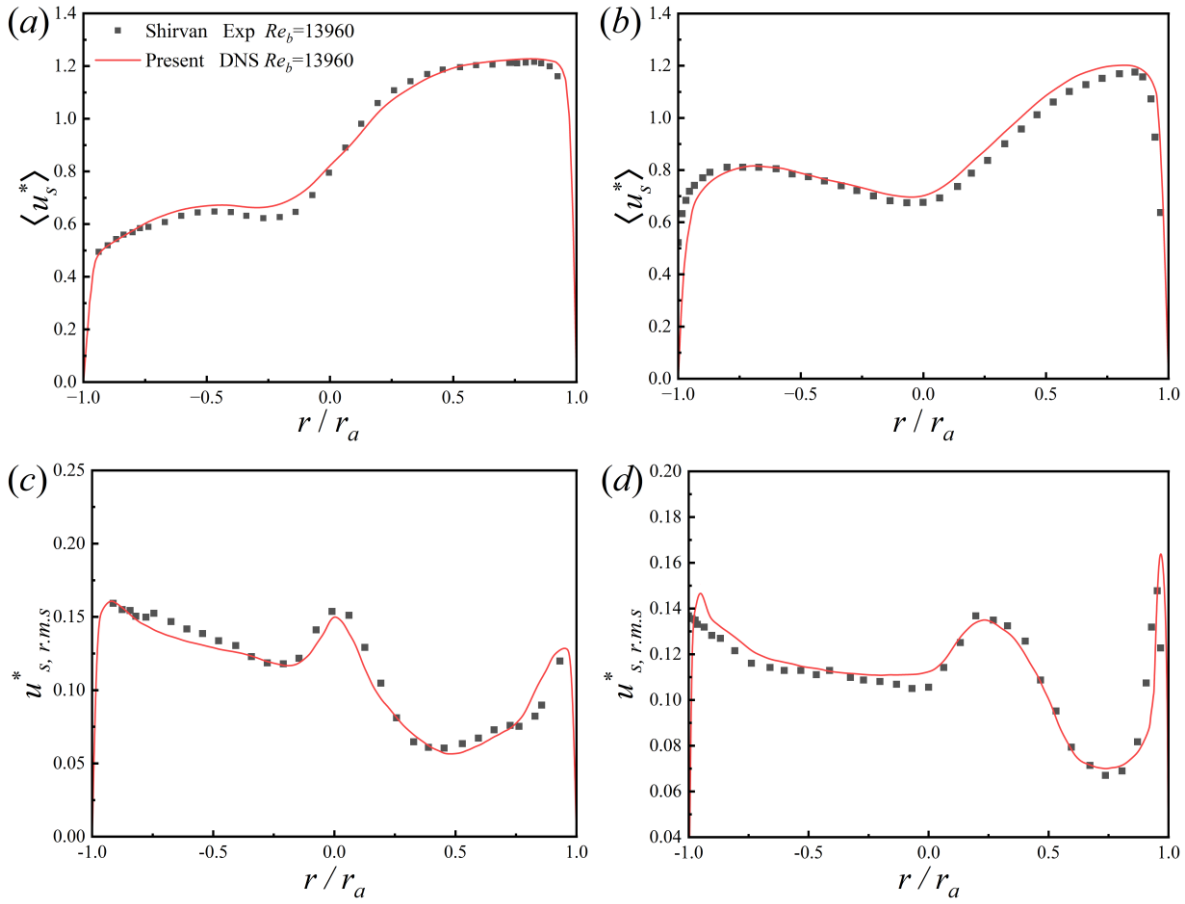

Figure 5. Velocity statistics in the pipe bend at $Re_b = 13{,}960$ compared with the data of Shirvan [4]: (a) mean velocity at plane $\Delta s = 0.5d$, (b) mean velocity at plane $\Delta s = 1.5d$, (c) r.m.s. fluctuating velocity at plane $\Delta s = 0.5d$, and (d) r.m.s. fluctuating velocity at plane $\Delta s = 1.5$.

With the attainment of statistical stability and validation of the single-phase flow field, a volume fraction (up to 10^{-3}) of particles was injected into the flow. Given this volume fraction, the intrinsic structure of turbulence is bound to be altered due to the presence of the solid particles. Considering the feedback forces of particles on the fluid therefore becomes imperative. To the authors' knowledge, no previous DNS study of a

particle-laden flow in a 90º pipe bend has employed two-way coupling between the particles and the fluid flow. The first- and second-order velocity statistics are considered primarily with the results presented in Figs. 6 and 7. Note that these fluid statistics were gathered after the particle-laden flow reached a statistically stationary state, which can be seen in the results of Fig. 8. The particle concentration achieved steady state after approximately $25\Delta t^*$, with statistics gathered subsequently for a duration of $120\Delta t^*$.

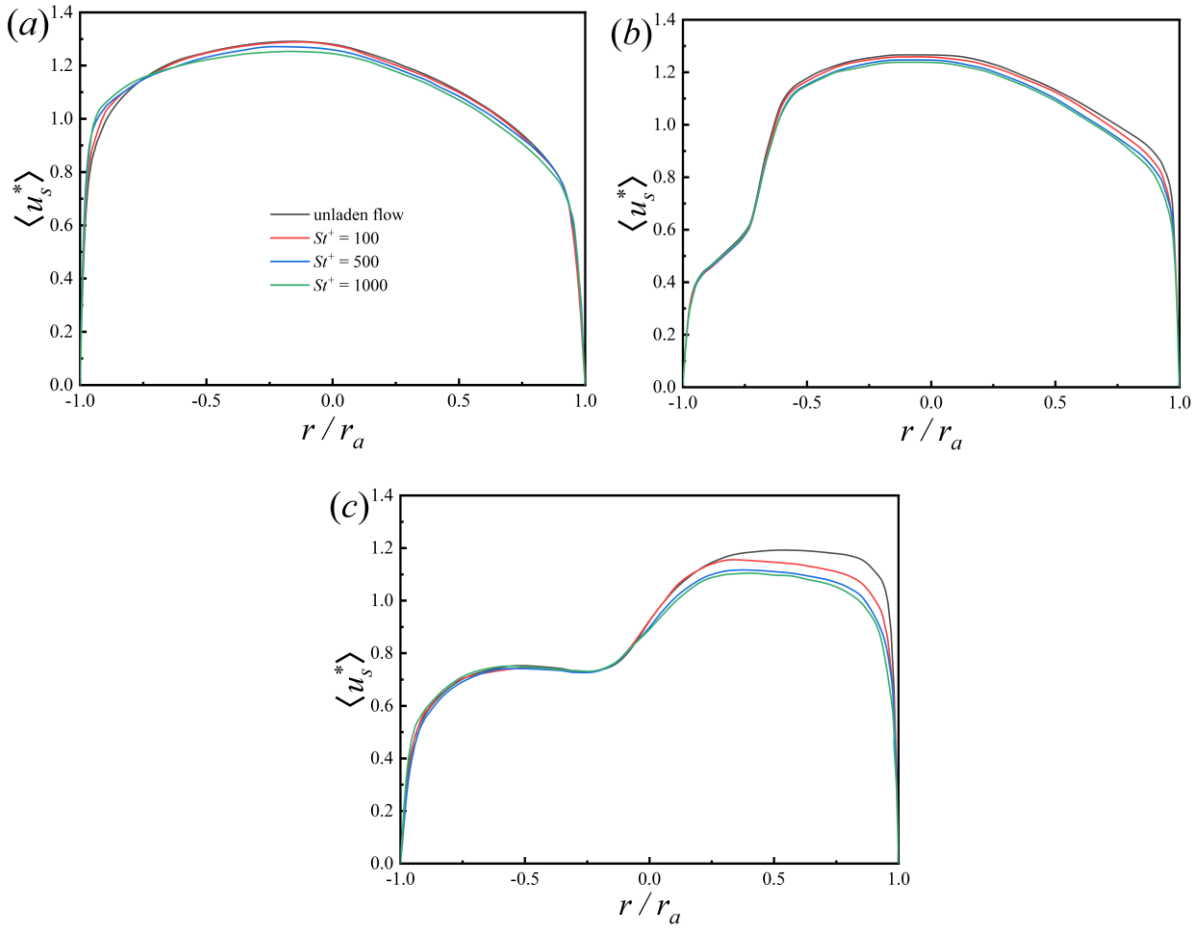

Figure 6. Mean streamwise velocity of carrier phase at different orientations on the vertical plane through the pipe bend at: (a) $\theta = 0°$, (b) $\theta = 45°$, and (c) $\theta = 90°$.

Figure 6 shows the mean streamwise velocity at three orientations on the vertical

plane through the pipe bend. The modulation effect of the particles on the first-order velocity statistics of the fluid flow is observed to be different near the inner and outer walls. In general, the mean velocity near the inner wall increases, while that near the outer wall decreases, with increasing particle Stokes number. According to previous studies on turbulence modulation in wall-bounded turbulent flows, it has been reported that the presence of particles tends to dampen the mean velocity [42-44] because the presence of particles induces resistance to the flow. This effect is related to the distribution of particles. In typical wall-bounded turbulence, due to the turbophoresis effect, particles tend to accumulate close to the wall, leading to a decrease in the mean velocity in that region and an increase in the mean velocity in the core of the flow where fewer particles are present. However, the fluid in the pipe bend exhibits strong spatial sensitivity. Additionally, when particles exit the flow field, they re-enter at random locations on the injection plane upstream of the bend, making it difficult for turbophoresis to drive particles near the wall over small timeframes. In the present study, we aim to generate fundamental knowledge surrounding the trajectories of particles entering the bend from the inner, centre and outer pipe bend regions, and therefore this setup is idealised for focusing the analysis. That said, it is evident that for long pre-bend timescales turbophoresis may occur before the bend (particularly for particles with increased Stokes numbers). This will be considered in future work, but in the present study, as noted, the focus was on isolating the impact of the bend flow itself on particle distributions. As a consequence of this approach, a significant number of particles continue to disperse in the central region of the pipe. Mortimer et al. [18] reported in

channel flows that turbulence modulation exhibits two scales of time sensitivity. The first is the initial timescale associated with the initial reaction of the flow to the injection of the particulate phase, with the second a much longer timescale wherein turbophoresis slowly redistributes the particles towards the wall-region. Within the $2d$ length upstream of the bend, the effect of turbophoresis is not particularly evident. Gravity results in more particles on the lower side (outer bend), hence causing a slight increase in the mean velocity on the inner side and a decrease on the outer wall. Additionally, in the bend, due to centrifugal forces, larger particles tend to migrate towards the outer wall, leading to significantly higher particle concentrations near that wall compared to the inner wall. The presence of these particles contributes to the deceleration of the continuous phase flow. This effect is most notable in the plane at θ=90°, and larger particles have a more pronounced deceleration effect on the fluid.

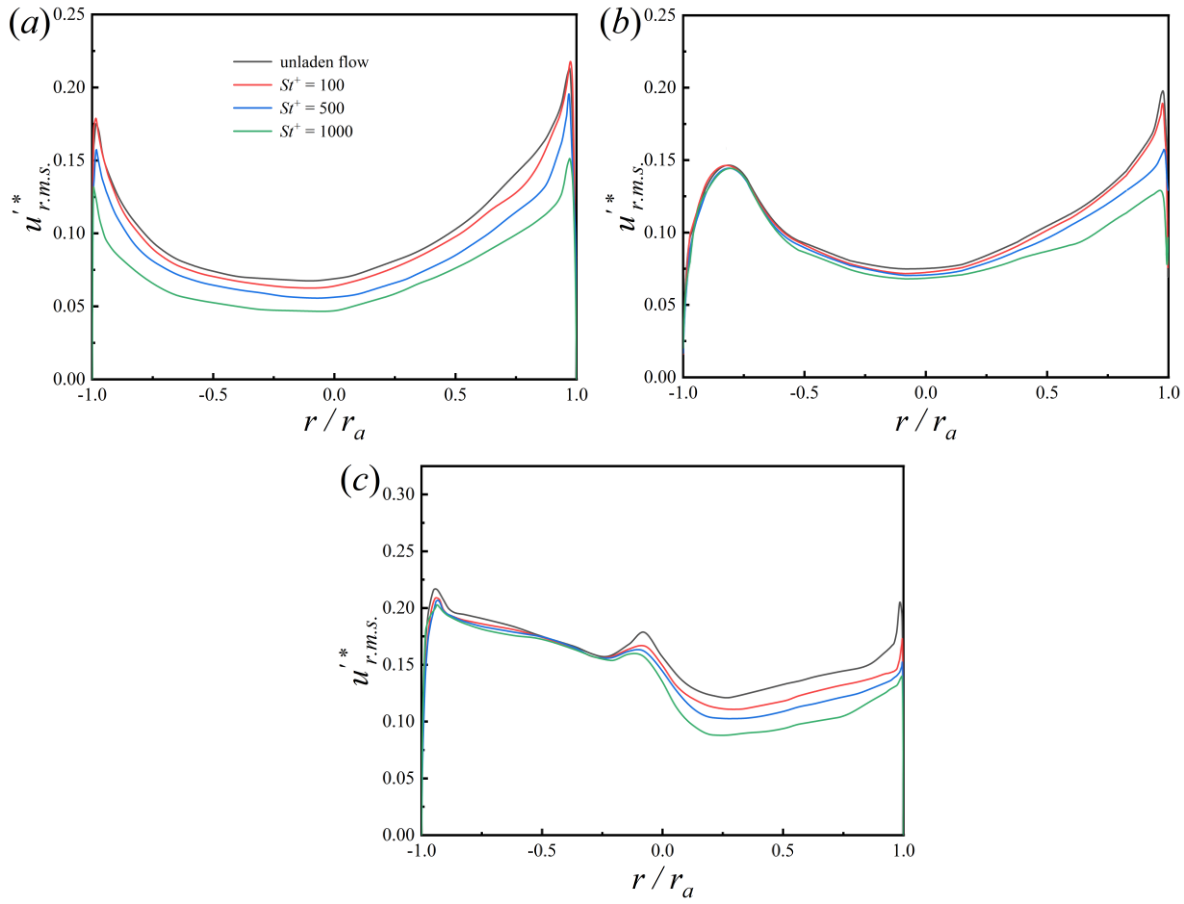

Figure 7. Normal stresses at different orientations on the vertical plane through the pipe bend at: (a) $\theta = 0°$, (b) $\theta = 45°$, and (c) $\theta = 90°$.

Figure 7 displays turbulent velocity fluctuations at the same three orientations as in Fig. 6. It is evident that the influence of the particles on the r.m.s velocities of the fluid flow is significantly greater than their effect on the mean velocity. For the three inertial particles studied, the suppression of turbulence is stronger with an increase in St^+. From a spatial evolution perspective, the peak value of the r.m.s velocity on the inner wall of the pipe bend gradually shifts outward. At $\theta = 90°$ in particular, this peak value moves to the approximate centre of the pipe, forming a new peak in the near-wall region, with turbulence suppression in the outer region $(r/r_a) \in (0 - 1)$ greater

than that in the inner region.

3.2 Particulate phase

The particles were injected into the flow field of the fully developed turbulent flow, distributed uniformly in the radial (r), azimuthal (φ), and streamwise (s) directions. Their initial velocity was set equal to the local flow velocity and a total of three particle populations with varying St^+ values were considered, as shown in Table 2. The density ratio remained fixed at 694, and different St^+ values for each particle population were achieved by adjusting the radius of the particles. We chose three relatively large particles with Stokes numbers ranging from 100 to 1000 since, as previously noted, earlier research has primarily focused on low Stokes numbers particles, and since such St^+ values are directly relevant to nuclear waste processing operations, of specific interest in the present work.

3.2.1 Temporal convergence

The instantaneous particle concentration *C*, i.e. the number of particles per unit volume, normalized by the bulk particle concentration in the computational domain was tracked in the viscous sublayer ($\delta^+ \leq 5$, corresponding to $(1 - r/r_a) \leq 0.012$). Monitoring of this quantity helps identify when particle dispersion reaches a statistically stationary state.

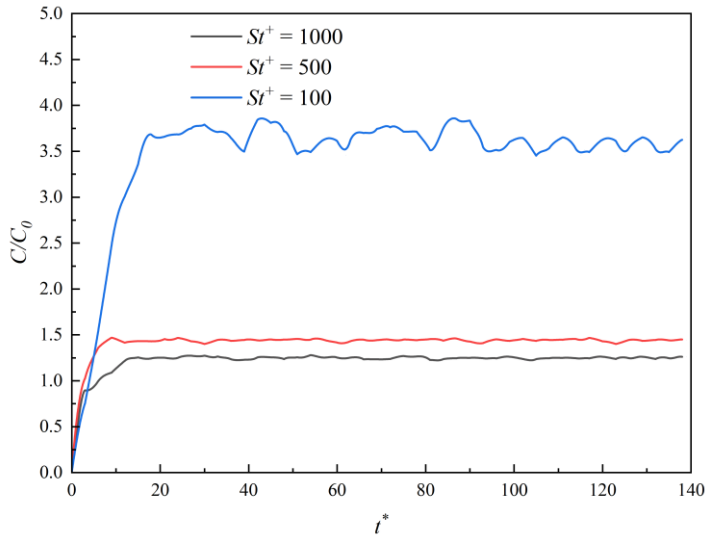

Figure 8. Instantaneous particle concentration for two-way coupling in the viscous sublayer $(\delta^+ \leq 5,\ (1 - r/r_a \leq 0.012)$ normalised by the mean particle concentration in the domain as a function of time for three particle populations.

Typically, near-wall concentrations rise due to particle turbophoresis until they saturate, indicating a statistically steady state in the process. This effect is visible in Fig. 8. Additionally, during the initial simulation stage, the random seeding of particles results in fewer particles near the walls, causing most particles to be distributed in the core region of the pipe due to the increased volume at that location. Hence, the initial concentration of particles near the walls is relatively low. Subsequently, a rapid increase in particle concentration near the walls occurs due to the turbophoretic effect. Once concentrations have plateaued, fluctuations in particle concentration values can be observed. Noorani et al. [21] and Yan et al. [22] reported a similar phenomenon. Noorani et al. [219] studied St^+ values ranging from 1 to 100, noting that larger particles exhibited greater oscillation amplitudes but shorter oscillation periods within this range. They

attributed this behaviour to the influence of secondary flows in the pipe bend. Inertial particles, due to centrifugal forces and the presence of Dean vortices directing particles from the inner to the outer wall in the central region of the pipe, are thus propelled towards the outer wall, leading to their accumulation there. These particles then experience redirection by the secondary flow from the outer to the inner wall along the sidewalls, re-entering the central flow region. Similar oscillations in particle concentration are observed in the present results for $St^+ = 100$, but for the other heavier particles, these oscillations were mitigated. The increase in particle concentration in the initial stage is caused by turbophoresis. In addition, the reason for the higher particle concentration at a lower Stokes number is related to turbophoresis, particle inertia and particle-wall collisions. The reason for the oscillation of this temporal evolution is that the secondary flow is not statistically stationary which is caused by turbulence as well as by particles being transported between the near-wall region and the central region of the flow, which is mainly related to the turbulence, secondary flow and particle-wall collision. Particle motion in a pipe with a bend is influenced by multiple factors, including geometry-induced centrifugal acceleration, Dean vortices, turbulent dispersion, and particle-wall collisions. The reason for this observation regarding the heavier particles is considered further below.

3.2.2 Particle spatial distribution

To analyze particle transport in the pipe, the instantaneous particle distribution for the various particle sizes and azimuthal angles is shown in Figs. 9 and 10. Note that the azimuthal angle, φ and the streamwise centre-axis distance, s, are illustrated in Fig.

1. Figure 9 displays the instantaneous particle distribution across the whole computational domain after reaching a statistically stable state, with the right half of each plot providing an open-cut view of the particles distributed in the viscous sublayer (y^+ <5). The three-dimensional views of the different inertial particles in Fig. 9 reveal that, for the considered particle types, all form regions where no particles are present, known as particle void regions. Among these, the particle void regions for the $St^+ =$ 500 and 1000 particles are notably larger than that for the $St^+ = 100$ particles. The response of the two larger inertial particles to the turbulent flow is therefore significantly lower than that of the $St^+ = 100$ particles. In particular, they exhibit a weak response to small-scale turbulence, but the influence of the Dean vortices on these larger particles is clearly observable. Downstream of the bend, the particle distribution forms an x-shape which is more clearly visible for the $St^+ = 500$ and 1000 particles in the right hand plots of Fig. 9 showing the viscous sublayer distribution. Additionally, it is apparent that these larger particles do not exhbit any streakiness in their structure, unlike the $St = 100$ particles where such structures are clearly visible. In previous studies of wall-bounded turbulent flows, it has been frequently noted that particles tend to accumulate within the low-speed streaks of coherent structures close to solid surfaces, and this effect is sensitive to the Stokes number. For instance, in turbulent channel flows, Mortimer et al. [18] reported that particle streaks were most pronounced at approximately $St^+ = 25$. Lower Stokes number particles near the wall were uniformly distributed, making it almost impossible to identify their position within the low-velocity streaks. Also, as the Stokes number surpassed 25, the streaks started

to become less distinct because the particles began to decouple from the fluid motion and show little response to small scale turbulence. In terms of pipe bend flows, Noorani et al. [21] reported that, for a straight pipe, the particle streaky structure is homogeneously distributed over the pipe wall circumference, while in curved configurations, the particle streaks are not exclusively elongated in the axial direction but are also inclined azimuthally, pointing towards the inner bend. These streaks tended to aggregate at a certain angle, resembling structures akin to a fishbone. A similar phenomenon can also be observed in Fig. 9. Hence, in Fig. 9(a), streak-like structures of the lightest particles can be observed which also display an inclination in the azimuthal direction, attributable to the influence of the Dean vortices. In addition to causing the slanting of streaky structures in small particles, Dean vortices also contribute to the x-shaped distribution near the wall for the two larger particles.

Figure 10 shows the instantaneous particle distribution on cross-sectional planes at $\theta = 0°,\ 45°,$ and $90°$ in the curved pipe. On the planes at $\theta = 0°$, the distribution of the three types of particles is similar since the secondary flows have not yet formed as the flow and conveyed particles have not entered the curved pipe section. The particles are generally uniformly distributed within the pipe at this location. On the downstream planes, the shapes and sizes of the particle void regions can be observed more clearly. Noorani et al. [21] conducted an investigation of particle void regions in infinitely long curved pipes. Under the influence of stable Dean vortices in the pipes, void regions were positioned at the centre of the these vortices, and as the curvature of the pipe increased, these regions grew larger. In this study, where both particle inertia

and curvature (for a 90º pipe bend) are relatively high, and where stable Dean vortices cannot be formed, the particle void regions are located on the inner wall of the pipe, with particles predominantly accumulating on the pipe outer wall. Secondary flows along the sidewall push particles from the outer wall toward the inner regions of the pipe, resulting in small concentrations of particles near the inner wall and sidewall. However, it is noteworthy that this effect of the secondary flows does not apply to all types of particles considered. The $St^+ = 100$ particles are therefore pushed towards the vicinity of the inner wall. However, for the two larger inertial particles, the effect of the secondary flows is insufficient to drive them towards this location. Additionally, the plume pattern of particles reported by Noorani et al. [21] is not observed for the highest inertia particles considered here. Instead, near the outer wall, there is only a minor elevation in particle concentration caused by particle-wall collisions. Interestingly, for the $St^+ = 500$ and 1000 particles on the $\theta = 90°$ plane, a ring-shaped distribution is observed. This particle layering is attributable to collisions between the particles and the wall, and is commonly referred to as the "reflection layer." The existence of such layering in high inertia particle-laden flows was first identified by Huang et al. [45].

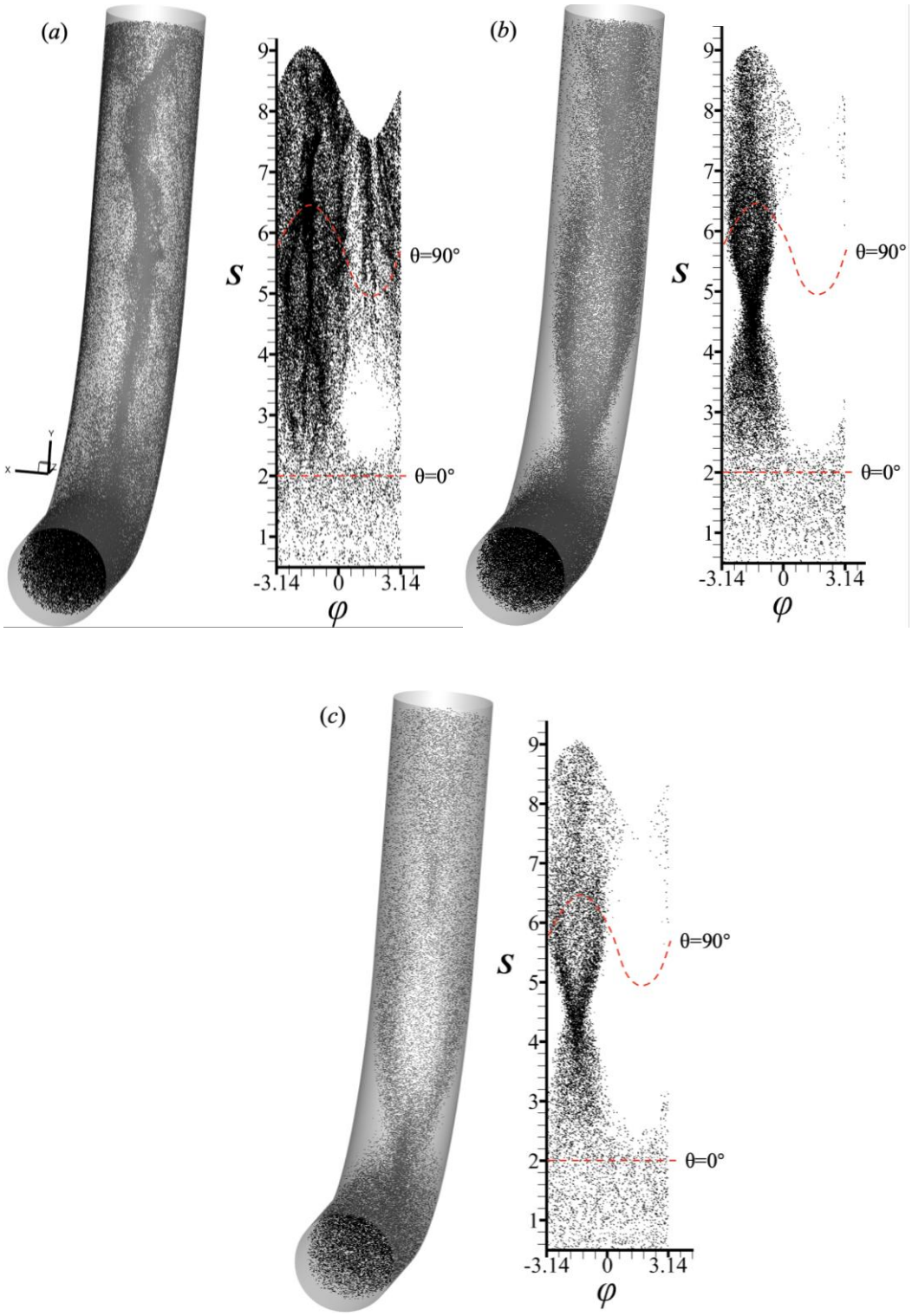

Figure 9. Instantaneous particle distribution in the whole computational domain and an open-cut view of the particles distributed in the viscous sublayer for: (a) $St^+ = 100$, (b) $St^+ = 500$, and (c) $St^+ = 1000$.

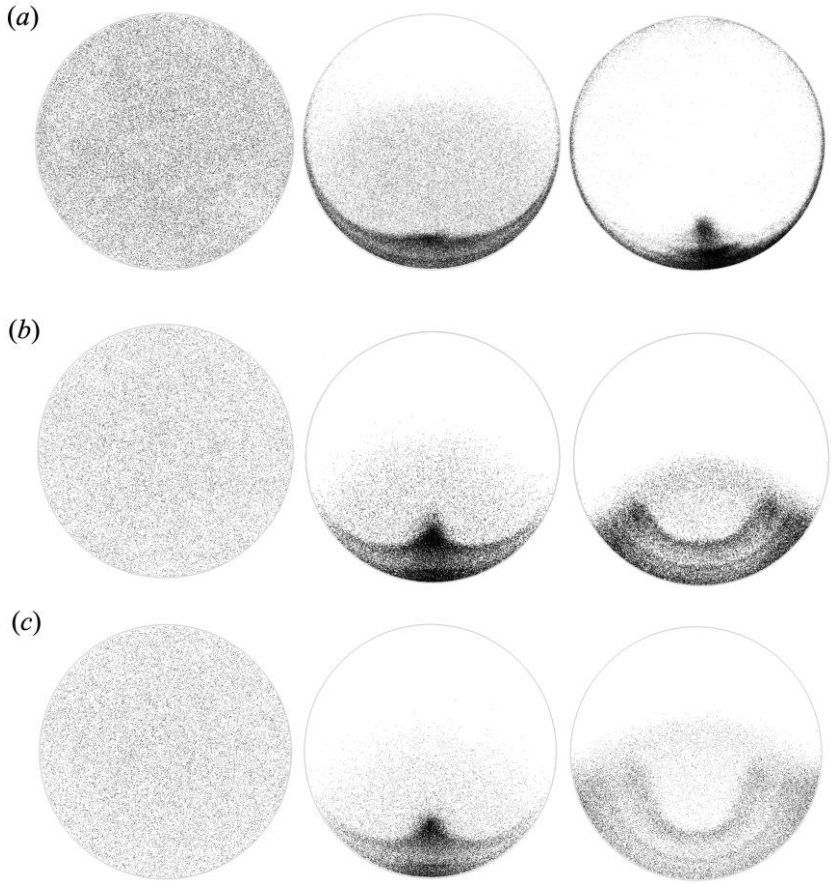

Figure 10. Instantaneous particle distribution on cross-sectional planes at $\theta = 0°$, 45°, and 90° (from left to right) for: $St^+ = 100$, (b) $St^+ = 500$, and (c) $St^+ = 1000$.

In addition to this qualitative characterization of particle distribution, we additionally quantify the distribution using probability density functions (PDFs) on the vertical plane through the pipe, as shown in Fig. 11. Consistent with most wall turbulence, the particles tend to accumulate in the near-wall region. At $\theta = 0°$, apart from higher values near the wall, the particle distribution is relatively uniform over the rest of the pipe. As θ increases, the inner bend region becomes almost totally depleted

of particles, forming a particle void region. At $\theta = 45°$, the void regions for the $St^+ =$ 500 and 1000 particles are comparable and larger than that generated by the $St^+ =$ 100 particles. However, the size of the void region does not necessarily increase with St^+. At $\theta = 90°$, the void region of the $St^+ = 500$ particles is now larger than that of the $St^+ = 1000$ particles. This is likely due to the heaviest particles bouncing back towards the centre of the pipe after hitting the wall. Additionally, in Figs. 11(b) and 11(c), multiple PDF peaks near the outer wall of the pipe are evident, corresponding to the reflection layers seen in Fig. 10. These reflection layers occur due to particles impacting the outer wall at significant velocities, resulting in them bouncing off the wall through elastic collisions. The distance of the rebound away from the wall into the rest of the pipe is mainly dictated by the incoming velocity of the particles. When the incoming particles maintain a sufficiently high and relatively consistent velocity, such particle layers become observable. These results suggest that heavier particles lead to a more pronounced rebound effect. Therefore, the reflection layers are more visible for heavier particles. This observation was also noted by Huang and Durbin [45] in the vicinity of the outer bend of a highly curved S-shaped channel containing heavy particles.

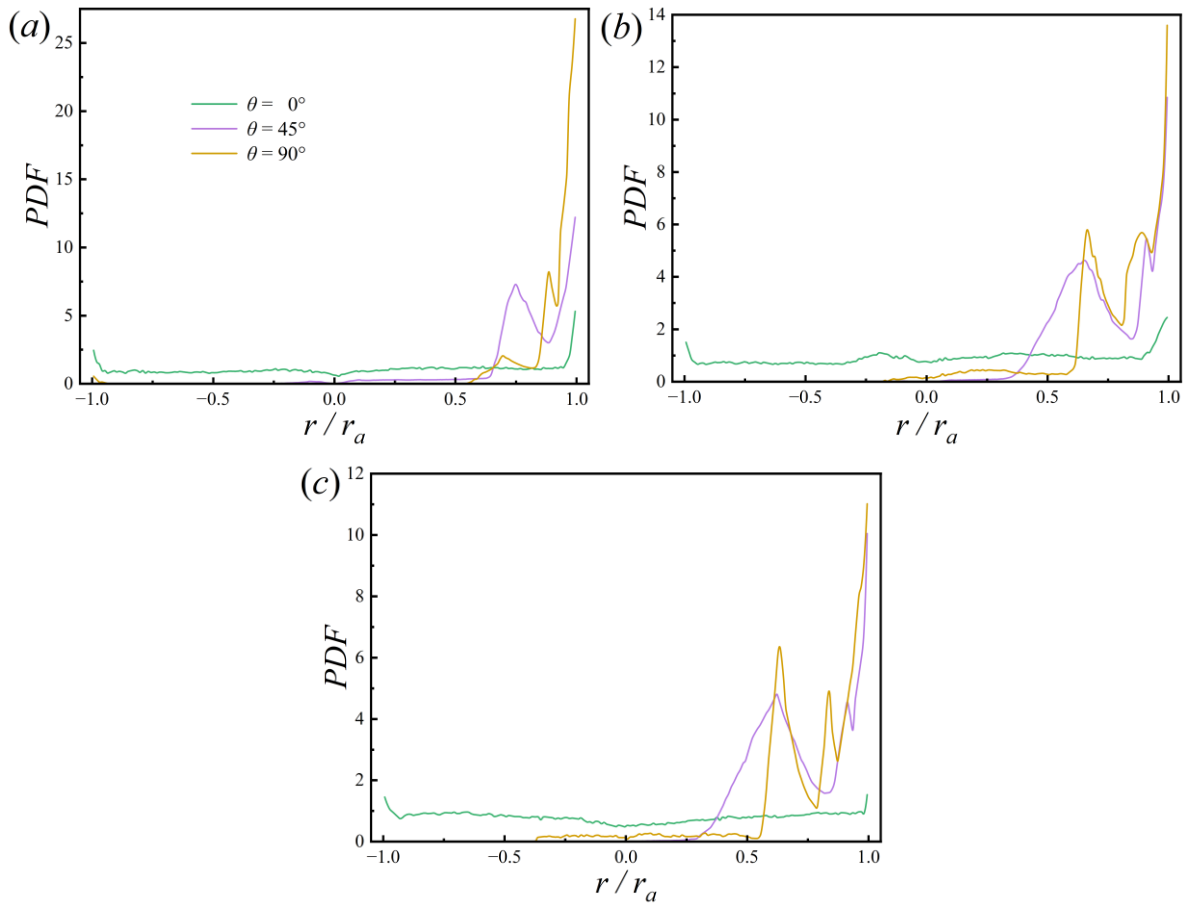

Figure 11. PDF of particle distribution on the vertical plane through the pipe at $\theta = 0°, 45°,$ and $90°$ for: (a) $St^+ = 100$, (b) $St^+ = 500$, and (c) $St^+ = 1000$.

3.2.3 Particle velocities

To quantitatively understand particle transport in the pipe bend, we consider the first and second order Eulerian particle velocity statistics derived from Lagrangian particle tracking data. Figure 12 gives the mean particle streamwise velocity on the vertical plane through the pipe. As expected, for the three high inertia particles simulated in this study, the particle streamwise velocity is slower than that of the fluid in the cross-section at $\theta = 0°$ and $45°$ (cf. Fig. 6). A clear reduction can also be seen in Fig. 12 (a, b) with increasing St^+. As the particle inertia increases at $\theta = 45°$, the

particle void region expands, and the position of the peak in the mean streamwise velocity shifts toward the outer bend. However, at $\theta = 90°$ the results deviate significantly from those at $\theta = 45°$. From Fig. 12(c), therefore, the largest and smallest particle void regions appear for the lightest and heaviest particle cases, respectively, which is different from what was observed in the upstream section of the curved pipe. The reason for this is attributable to the effects of particle-wall collisions. The heaviest particles with high inertia, upon collision with the wall, manage to counteract the action of the fluid flow and move towards the inner side of the bend, resulting in a smaller void region. In contrast, the smallest particles respond more quickly to the small-scale flow structures and tend to accumulate mostly on the outer side of the pipe, although clearly some particles are still present close to the inner wall. Additionally, the extent of particle velocity attenuation, relative to upstream locations, is highest for the $St^+ = 100$ particles, followed by $St^+ = 1000$ and with the $St^+ = 500$ particles exhibiting the least decay. This is closely related to the locations at which particle-wall collisions occur, and hence is associated with the different particle Stokes numbers.

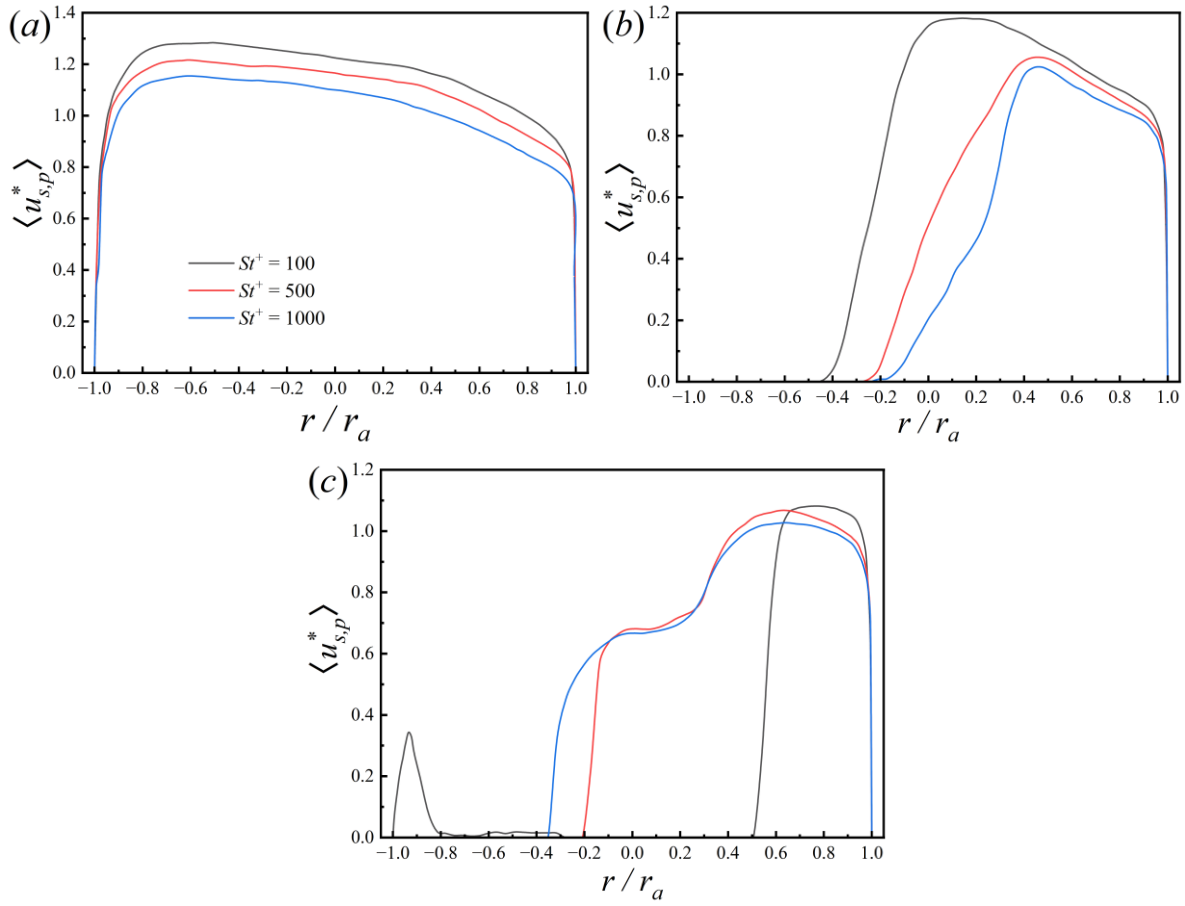

Figure 12. Mean particle streamwise velocity on the vertical plane through the pipe at: (a) $\theta = 0°$, (b) $\theta = 45°$, and (c) $\theta = 90°$.

Figure 13 gives the mean particle radial velocity on the vertical plane through the pipe. Unlike the streamwise velocity of the particles that remains directionally the same after a wall collision, the radial component is reversed. Therefore, some interesting phenomena arise. At $\theta = 0°$, the radial velocity overall resembles that in a straight pipe, but the curvature of the pipe still has some influence, causing a slight asymmetry close to the inner and outer wall, with higher peaks near the inner side, particularly for the two larger particles. The Stokes number effect on particle velocity reduction is similar to previous results, with heavier particles experiencing a more significant reduction in

velocity. At the downstream locations, there are instances of reversed radial velocities and local peaks due to particle-wall collisions. For the heavier $St^+ = 500$ and 1000 particles, there is a sharp drop in the radial velocity at $r/r_a \approx 0.6$, with values becoming negative, and with the positions of the minimum values corresponding to the maximum values of the particle concentration in Fig. 10(b). For the lightest $St^+ = 100$ particles, the peak particle concentration at $\theta = 45°$ is around $r/r_a \approx 0.8$, with a minimum in the radial particle velocity occurring at the same position, although this is notably less than for the other two particles. At $\theta = 90°$, both heavier particles exhibit multiple peaks, with slightly different positions. Furthermore, it is worth noting that for the lightest particles, around $r/r_a = -0.9$, negative values of the radial velocity occur, indicating the statistical occurrence of particles moving from the inner to the outer wall. This corresponds to particles being driven along the side wall from the outer to the inner wall in Fig. 10, converging at an inner wall stagnation point before being pushed back towards the pipe centre.

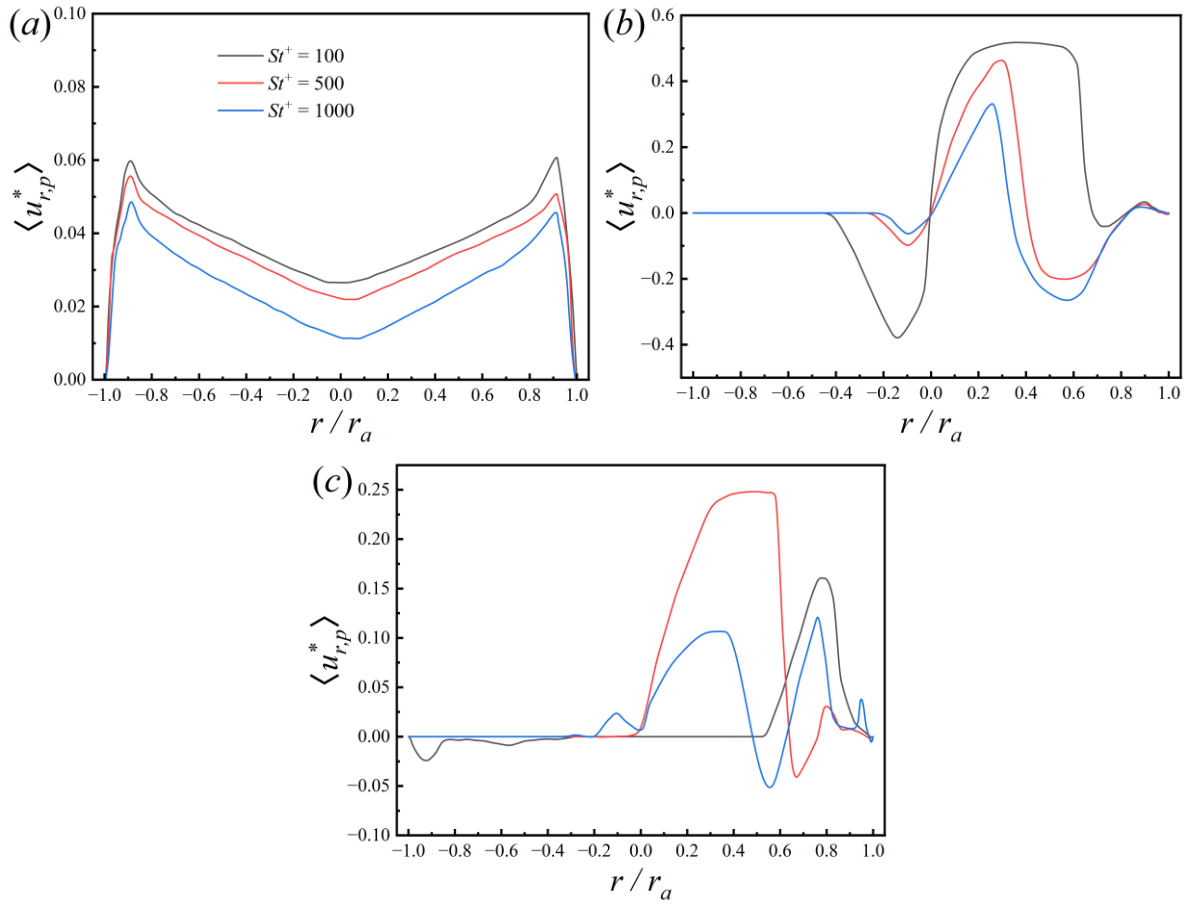

Figure 13. Mean particle radial velocity on the vertical plane through the pipe at: (a) $\theta = 0°$, (b) $\theta = 45°$, and (c) $\theta = 90°$.

The influence of inertia on particle velocity fluctuations is shown in Figs. 14 and 15 which give the root mean square of the streamwise and radial velocity fluctuations, respectively, on the vertical plane through the pipe. For the streamwise component across the three orientations, the r.m.s. velocity of the inertial particles is dampened at all locations with increasing Stokes number. This aligns with findings indicating lower particle fluctuations and reduced turbulence intensities in most regions of the bend reported by Noorani et al. [46], although the slight enhancement of $u^*_{s,r.m.s,p}$ in the outer bend region reported by the latter authors is not observed in this study. However, in this

study, the particles simulated have considerable inertia, and the reduction in turbulence levels can be explained by the particles filtering out the fastest turbulent motions [42].

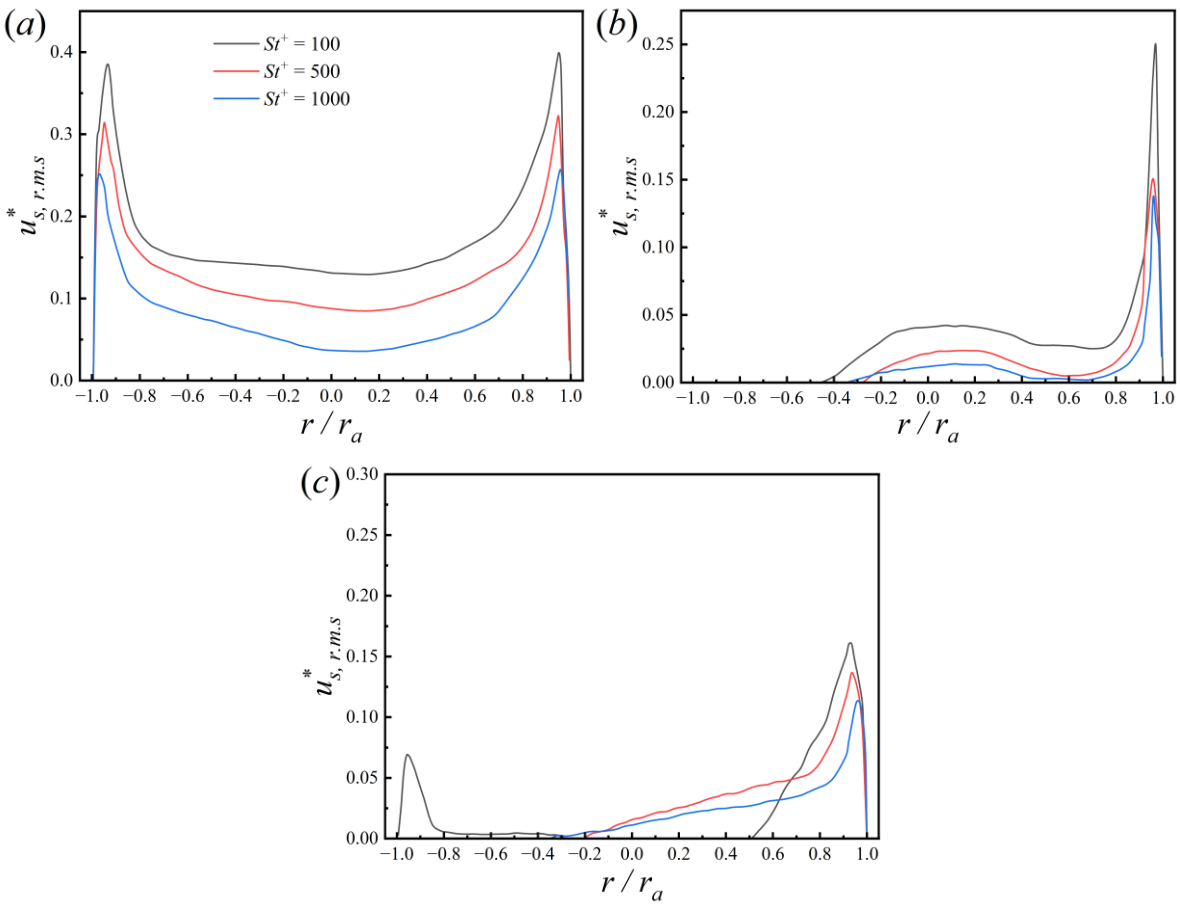

Figure 14. Particle streamwise r.m.s velocity on the vertical plane through the pipe at: (a) $\theta = 0°$, (b) $\theta = 45°$, and (c) $\theta = 90°$.

At θ=0°, the r.m.s. of the radial velocity fluctuations qualitatively resembles the radial mean velocity profiles, but now with a more significant asymmetry between the inner and outer walls. For the radial velocity fluctuations at $\theta = 45°$ and $90°$, a series of peaks can be observed in the outer bend region, again similar to the results for the radial mean velocity. However, what is intriguing is that the maxima in the r.m.s. values

roughly correspond to minima in the mean velocity profiles. This is attributable to the formation of the reflection layer due to particle-wall collisions. In these regions, therefore, the heavier particles experience reflections at the wall, leading to particles moving both towards the outer wall and towards the pipe centre. More specifically, the radial velocity of most particles is directed from the inner to the outer wall before collisions with the outer wall reverse that velocity and direct particle motion towards the centre of the pipe. These particles in the reflection layer with a radial velocity directed away from the outer wall result in a cancellation effect on the mean radial velocity. Therefore, at the position of the reflection layer, there is a minimum in the mean radial velocity and a peak value of the r.m.s of radial velocity fluctuations. In regions without a reflection layer, from the pipe centre to the inner wall, the fluctuations in radial velocity are comparatively low, and the radial (wall-normal) mean particle velocity balances the drag on the particles from centrifugal forces with turbophoretic drift towards the inner bend wall, thereby reducing the radial intensity of turbulence. Within particle void regions there are, however, insufficient particle samples, resulting in an inability to produce reliable statistical particle velocity data in those regions.

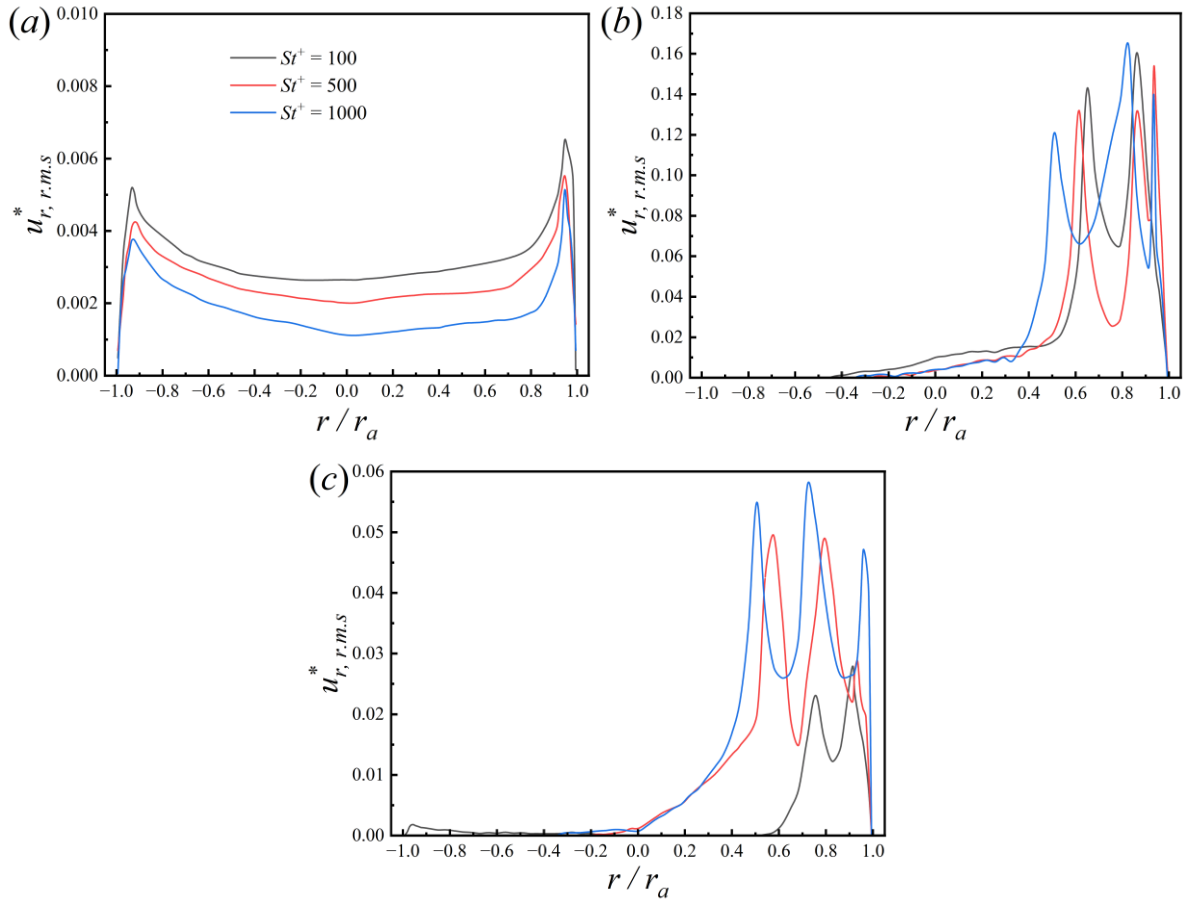

Figure 15. Particle radial r.m.s velocity on the vertical plane through the pipe at: (a) $\theta = 0°$, (b) $\theta = 45°$, and (c) $\theta = 90°$.

Based on the above analysis, particle-wall collisions are important for particle transport in pipes with a bend, especially for particles with high inertia. Figure 16 shows heat maps of particle-wall collisions frequency. For the lightest particles, collisions mainly occur after $\theta = 60°$, and the collision positions are mostly concentrated near the vertical plane through the pipe. The heat maps of the other two larger particles are relatively similar, with the x-shaped collision concentration areas corresponding to the similarly shaped particle distributions noted earlier. Also in agreement with previous findings, the centre of the x-shaped pattern is located at approximately $\theta = 30°$, with

these high collision frequency locations occurring significantly upstream of those of the $St^+ = 100$ particles.

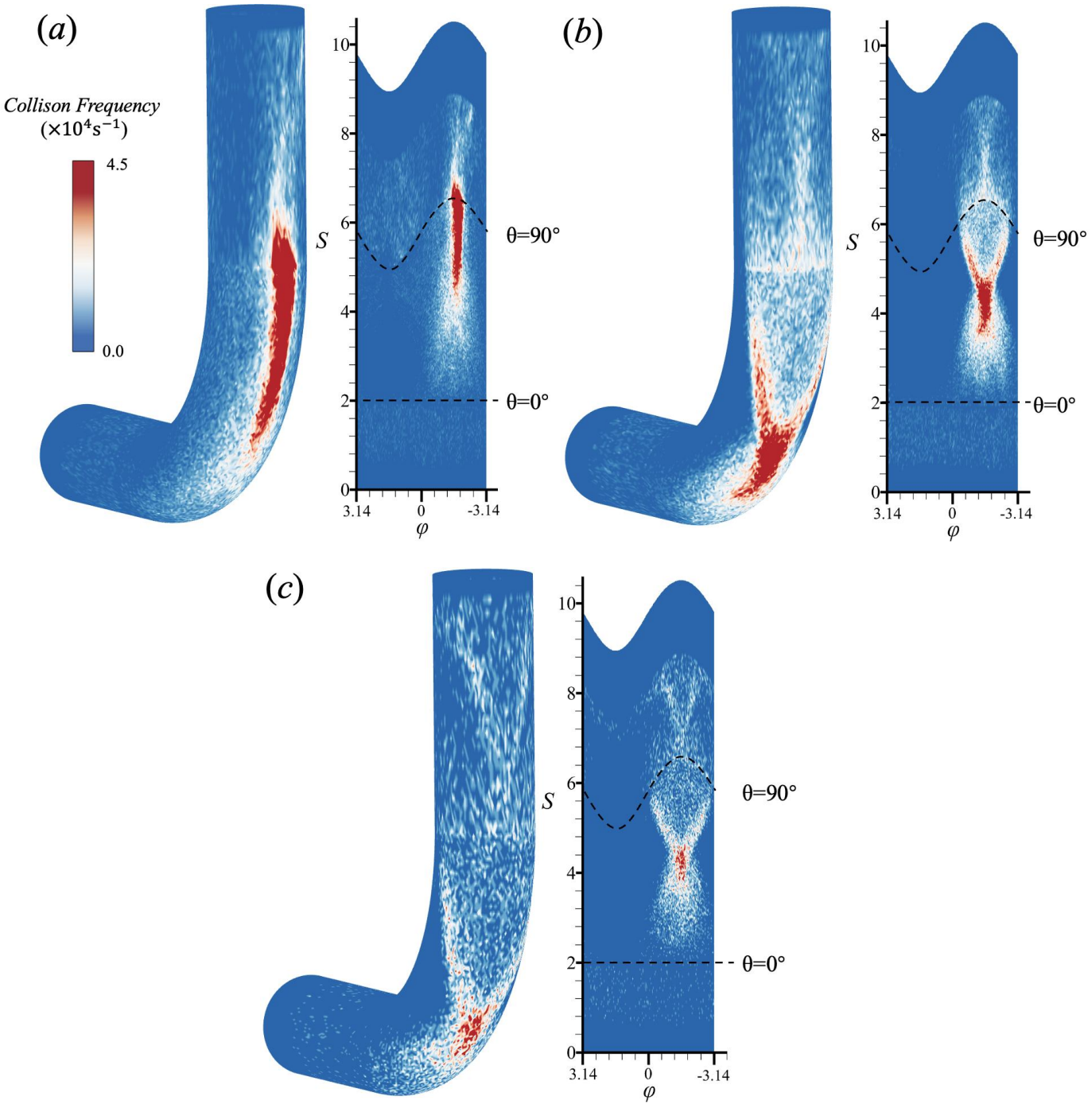

Figure 16. Particle-wall collisions frequency in the pipe bend for: (a) $St^+ = 100$, (b) $St^+ = 500$, and (c) $St^+ = 1000$.

4. Conclusions

In this work, DNS of particle-laden flows has been performed to investigate for the first time the interactions between turbulence and particle motion in a spatially developing turbulent 90º pipe bend flow using a two-way coupled Eulerian-Lagrangian point-particle approach. The simulations were conducted at a moderate Reynolds number and high curvature, corresponding to $Re_b = 13{,}960$ and $De = 6{,}350$. The particle Stokes numbers, St^+, considered were 100, 500 and 1000. The implementation of the numerical simulation was validated against available experimental data for the single-phase flow.

The turbulence statistics of the carrier phase and the influence of large inertial particles on them has been analysed. Turbulence modulation results show that the presence of particles causes the mean velocity to decrease in the outer bend and slightly increase in the inner bend regions. Also, the influence of the velocity fluctuations on the particles is weakened as the inertia of the particles increases. This modulation effect is shown to be closely related to the distribution of particles in the pipe bend. The pipe curvature therefore drastically changes the various particle distributions due the centrifugal force and secondary flow motion. Particles in the pipe largely accumulate near the outer wall, causing a dampening of the flows first and second order turbulence statistics.

In terms of the particulate phase dynamics, there are two interesting phenomena occurring in the high curvature 90º bend and large inertial particle-laden flow considered. One is the emergence of particle void regions close to the inner bend of the

pipe, and the other is the presence of particle reflection layers near the outer bend. Particles in the pipe with a bend are projected to the outer wall of the bend due to the centrifugal force and gather in large quantities in this region. Some particles with high inertia rebound back to the central area of the pipe after hitting the wall, whereas those with lower inertia are subsequently affected by the secondary flows. When the fluid provides them with sufficient centripetal force, these particles are driven by the secondary flows along the side walls to the inner wall and converge. They then travel to the stagnation point on the inner wall and resuspend within the central region of the pipe. The existence, shape and size of the particle void regions is mainly related to these two effects. The formation of the reflection layer is also caused by particle-wall collisions, which is consistent with the study of particle transport by Noorani et al. [21].

The two phenomena mentioned above also play an important role in the statistics of particle velocities. In particle void areas, the particle statistics exhibit lower accuracy in these regions of smallest concentration where insufficient particle samples are available. At the position of reflection layer, the peak value of the particle concentration and its radial velocity fluctuation, and the minimum value of the mean particle radial velocity, occur. This is effect is due to a reversal in the radial velocity of the particles after they collide with the outer wall of the pipe, which is cumulatively offset by the original particle velocity.

The present study serves as a dependable foundation for conducting subsequent theoretical investigations into the impact of curvature on turbulent wall-bounded particle-laden flows. With further resources and investigation, the effects of pre-bend

particle transport mechanisms such as turbophoresis and preferential concentration should be examined in order to determine how emergent effects modify the behaviour of the particles as they navigate the bend, and hence what the further implications are for turbulence modulation.

Data Availability

The data supporting the findings of this study are available from the corresponding author upon reasonable request.

Acknowledgements

The authors gratefully acknowledge the financial support from the China Scholarship Council. The computations were performed on the ARC facilities of HPC services at the University of Leeds.

References

1. P. Bradshaw, and A. D. Young, *Effects of streamline curvature on turbulent flow* (Agard Paris).
2. A. Kalpakli Vester, R. Örlü, and P. H. Alfredsson, "Turbulent flows in curved pipes: Recent advances in experiments and simulations," Applied Mechanics Reviews **68**, 050802 (2016).
3. K. Sudo, M. Sumida, and H. Hibara, "Experimental investigation on turbulent flow in a circular-sectioned 90-degree bend," Exp. Fluids **25**, 42 (1998).
4. S. Sattarzadeh Shirvan, "Experimental study of complex pipe flow," Royal Institute of Technology, Stockholm, 2011.
5. H. Takamura, S. Ebara, H. Hashizume, K. Aizawa, and H. Yamano, "Flow

visualization and frequency characteristics of velocity fluctuations of complex turbulent flow in a short elbow piping under high reynolds number condition," J. Fluids Eng.-Trans. ASME **134**, (2012).

6. L. H. O. Hellström, M. B. Zlatinov, G. Cao, and A. J. Smits, "Turbulent pipe flow downstream of a 90º bend," J. Fluid Mech. **735**, R7 (2013).
7. A. Kalpakli, and R. Örlü, "Turbulent pipe flow downstream a 90° pipe bend with and without superimposed swirl," Int. J. Heat Fluid Flow **41**, 103 (2013).
8. C. A. Ribeiro Duarte, F. J. de Souza, R. d. V. Salvo, and V. F. dos Santos, "The role of inter-particle collisions on elbow erosion," Int. J. Multiph. Flow **89**, 1 (2017).
9. J. Kim, M. Yadav, and S. Kim, "Characteristics of Secondary Flow Induced by 90-Degree Elbow in Turbulent Pipe Flow," Eng. Appl. Comp. Fluid Mech. **8**, 229 (2014).
10. S. Wallin, and A. V. Johansson, "Modelling streamline curvature effects in explicit algebraic Reynolds stress turbulence models," Int. J. Heat Fluid Flow **23**, 721 (2002).
11. T. Hüttl, and R. Friedrich, "Influence of curvature and torsion on turbulent flow in helically coiled pipes," Int. J. Heat Fluid Flow **21**, 345 (2000).
12. T. J. Hüttl, and R. Friedrich, "Direct numerical simulation of turbulent flows in curved and helically coiled pipes," Computers & fluids **30**, 591 (2001).
13. A. Noorani, G. El Khoury, and P. Schlatter, "Evolution of turbulence characteristics from straight to curved pipes," Int. J. Heat Fluid Flow **41**, 16 (2013).
14. Z. X. Wang, Örlü, R., Schlatter, P., Chung, Y. M., "Direct numerical simulation of a turbulent 90 degrees bend pipe flow," Int. J. Heat Fluid Flow **73**, 199 (2018).
15. L. Hufnagel, J. Canton, R. Örlü, O. Marin, E. Merzari, and P. Schlatter, "The three-dimensional structure of swirl-switching in bent pipe flow," J. Fluid Mech. **835**, 86 (2018).
16. J. Young, and A. Leeming, "A theory of particle deposition in turbulent pipe flow," J. Fluid Mech. **340**, 129 (1997).
17. S. Balachandar, and J. K. Eaton, "Turbulent dispersed multiphase flow," Annu. Rev. Fluid Mech. **42**, 111 (2010).

18. L. F. Mortimer, D. O. Njobuenwu, and M. Fairweather, "Near-wall dynamics of inertial particles in dilute turbulent channel flows," Phys. Fluids **31**, (2019).
19. Y. Wang, M. Fairweather, L. F. Mortimer, Y. Zhao, and J. Yao, "Mechanisms of particle preferential concentration induced by secondary motions in a dilute turbulent square duct flow," Phys. Fluids **32**, 123313 (2020).
20. S. Vashisth, V. Kumar, and K. D. Nigam, "A review on the potential applications of curved geometries in process industry," Ind. Eng. Chem. Res. **47**, 3291 (2008).
21. A. Noorani, G. Sardina, L. Brandt, and P. Schlatter, "Particle transport in turbulent curved pipe flow," J. Fluid Mech. **793**, 248 (2016).
22. Y. Yan, Y. Zhao, J. Yao, and C.-H. Wang, "Investigation of particle transport by a turbulent flow through a 90° bend pipe with electrostatic effects," Powder Technol. **394**, 547 (2021).
23. Y. Yan, Y. Zhao, M. Liu, and J. Yao, "Reynolds number dependence of particle transport in a 90° bend with electrostatic effects," Particuology **77**, 91 (2023).
24. P. Fischer, J. Lottes, and S. G. Kerkemeier, *nek5000 Web page: https://nek5000.mcs.anl.gov/* (2008).
25. G. K. El Khoury, P. Schlatter, A. Noorani, P. F. Fischer, G. Brethouwer, and A. V. Johansson, "Direct numerical simulation of turbulent pipe flow at moderately high Reynolds numbers," Flow, Turbulence and Combustion **91**, 475 (2013).
26. J. Jimenez, and S. Hoyas, "Turbulent fluctuations above the buffer layer of wall-bounded flows," J. Fluid Mech. **611**, 215 (2008).
27. Y. Zhao, Y. Yan, X. Zhou, J. Yao, and C.-H. Wang, "Numerical investigation of electrostatic effect on particle behavior in a 90 degrees bend," Adv. Powder Technol. **32**, 810 (2021).
28. N. J. Georgiadis, D. P. Rizzetta, and C. Fureby, "Large-eddy simulation: current capabilities, recommended practices, and future research," AIAA journal **48**, 1772 (2010).
29. J. G. M. Kuerten, "Point-particle DNS and LES of particle-laden turbulent flow-a state-of-the-art review," Flow, Turbulence and Combustion **97**, 689 (2016).
30. V. Armenio, and V. Fiorotto, "The importance of the forces acting on particles in

turbulent flows," Phys. Fluids **13**, 2437 (2001).

31. A. Daitche, "On the role of the history force for inertial particles in turbulence," J. Fluid Mech. **782**, 567 (2015).
32. D. J. Vojir, and E. E. Michaelides, "Effect of the history term on the motion of rigid spheres in a viscous fluid," Int. J. Multiph. Flow **20**, 547 (1994).
33. J. Yao, and M. Fairweather, "Particle deposition in turbulent duct flows," Chem. Eng. Sci. **84**, 781 (2012).
34. M. Liu, J. Yao, and Y.-L. Zhao, "The dispersion of particles in turbulent semi-circular duct flows," Pet. Sci. **18**, 1240 (2021).
35. B. Wolde, L. F. Mortimer, and M. Fairweather, "Stokes Number Effects on Deposition in Particle‐Laden Turbulent Pipe Flows," Chemical Engineering & Technology **46**, 1351 (2023).
36. P. G. Saffman, "The lift on a small sphere in a slow shear flow," J. Fluid Mech. **22**, 385 (1965).
37. R. Mei, "An approximate expression for the shear lift force on a spherical particle at finite reynolds number," Int. J. Multiph. Flow **18**, 145 (1992).
38. C. T. Crowe, M. P. Sharma, and D. E. Stock, "The particle-source-in cell (PSI-CELL) model for gas-droplet flows," Journal of Fluid Engineering (1977).
39. A. Arsalanloo, and M. Abbasalizadeh, "Numerical study on deposition of particles in a 90 degrees bend in the presence of swirling flow using Eulerian-Lagrangian method," Powder Technol. **320**, 285 (2017).
40. S. Laín, and M. Sommerfeld, "Numerical prediction of particle erosion of pipe bends," Adv. Powder Technol. **30**, 366 (2019).
41. K. G. Bilde, K. Sørensen, and J. Hærvig, "Decay of secondary motion downstream bends in turbulent pipe flows," Phys. Fluids **35**, (2023).
42. M. Picciotto, C. Marchioli, and A. Soldati, "Characterization of near-wall accumulation regions for inertial particles in turbulent boundary layers," Phys. Fluids **17**, (2005).
43. X. Shao, T. Wu, and Z. Yu, "Fully resolved numerical simulation of particle-laden turbulent flow in a horizontal channel at a low Reynolds number," J. Fluid Mech.

693, 319 (2012).

44. Z. Lin, Z. Yu, X. Shao, and L.-P. Wang, "Effects of finite-size neutrally buoyant particles on the turbulent flows in a square duct," Phys. Fluids **29**, (2017).
45. X. Huang, and P. A. Durbin, "Particulate mixing in a turbulent serpentine duct," Phys. Fluids **24**, 013301 (2012).
46. A. Noorani, G. Sardina, L. Brandt, and P. Schlatter, "Particle Velocity and Acceleration in Turbulent Bent Pipe Flows," Flow Turbul. Combust. **95**, 539 (2015).